

Physical properties of the fullerene C₆₀-containing planetary nebula SaSt 2-3 [★]

Masaaki Otsuka^{1,2,†}

¹Okayama Observatory, Kyoto University, Kamogata, Asakuchi, Okayama, 719-0232, Japan

²Academia Sinica, Institute of Astronomy and Astrophysics, 11F Astronomy-Mathematics Building, NTU/AS campus, No. 1, Sec. 4, Roosevelt Rd., Taipei 10617, Taiwan, Republic of China

ABSTRACT

We perform a detailed analysis of the fullerene C₆₀-containing planetary nebula (PN) SaSt 2-3 to investigate the physical properties of the central star (BO-III) and nebula based on our own Subaru/HDS spectra and multiwavelength archival data. By assessing the stellar absorption, we derive the effective temperature, surface gravity, and photospheric abundances. For the first time, we report time variability of the central star’s radial velocity, strongly indicating a binary central star. Comparison between the derived elemental abundances and those predicted values by asymptotic giant branch (AGB) star nucleosynthesis models indicates that the progenitor is a star with initial mass of $\sim 1.25 M_{\odot}$ and metallicity $Z = 0.001/\alpha$ -element/Cl-rich ($[\alpha, \text{Cl}/\text{Fe}] \sim +0.3$ -0.4). We determine the distance (11.33 kpc) to be consistent with the post-AGB evolution of $1.25 M_{\odot}$ initial mass stars with $Z = 0.001$. Using the photoionisation model, we fully reproduce the derived quantities by adopting a cylindrically shaped nebula. We derive the mass fraction of the C-atoms present in atomic gas, graphite grain, and C₆₀. The highest mass fraction of C₆₀ ($\sim 0.19\%$) indicates that SaSt 2-3 is the C₆₀-richest PN amongst Galactic PNe. From comparison of stellar/nebular properties with other C₆₀ PNe, we conclude that the C₆₀ formation depends on the central star’s properties and its surrounding environment (e.g., binary disc), rather than the amount of C-atoms produced during the AGB phase.

Key words: ISM: planetary nebulae: individual (SaSt 2-3) — ISM: abundances — ISM: dust, extinction

1 INTRODUCTION

Mid-infrared (mid-IR) spectroscopic observations made by the *Spitzer*/Infrared Spectrograph (IRS, Houck et al. 2004) have recently detected fullerene C₆₀ and C₇₀ in a variety of space environments such as R Coronae Borealis stars (García-Hernández et al. 2011a), reflection nebulae (Sellgren et al. 2010), young stellar objects (Roberts et al. 2012), post asymptotic giant branch (AGB) stars (Gielen et al. 2011a,b), proto planetary nebula (PNe; Zhang & Kwok 2011), and PN (Cami et al. 2010; García-Hernández et al. 2010, 2011b, 2012; Otsuka et al. 2013, 2014, 2016). At the moment, PNe represent the largest fraction of fullerene detection; since the first detection of the mid-IR C₆₀ and C₇₀ bands in the C-rich PN Tc 1 by Cami et al. (2010), 24 fullerene-containing PNe have been identified in the Milky Way and the Large and Small Magellanic Clouds (LMC and SMC, respectively).

In general, C₆₀ PNe show very similar IR dust features and stellar/nebular properties; their mid-IR spectra display broad 6 – 9, 11, and 30 μm features in addition to C₆₀ bands at 7.0, 8.5, 17.4, and 18.9 μm , and they have cool central stars and low-excitation nebulae, indicating that their age after the AGB phase is very young (e.g., Otsuka et al. 2014). The excitation mechanisms (e.g., Bernard-Salas et al. 2012) and the formation paths (e.g., Berné et al. 2015; Duley & Hu 2012) are not well understood and are still a subject of debate. However, it remains unclear why these objects exhibit the C₆₀ features - is the span of time during which spectral features of C₆₀ are present a short-lived phase that all C-rich PNe go through, or are C₆₀ PNe distinct objects in terms of their stellar/nebular properties and/or evolution? This is directly linked to the question of how C₆₀ forms in evolved star environments. We would like to answer this fundamental question by investigating the physical properties of C₆₀ PNe and comparing them with non-C₆₀ PNe.

Amongst C₆₀ PNe, SaSt 2-3 (PN G232.0+05.7, Acker et al. 1992) firstly identified by Sanduleak & Stephenson (1972) is a particularly interesting object to that we should pay more attention. Otsuka et al. (2014) discovered C₆₀ bands in this PN for the first time. Surprisingly, the mid-IR C₆₀ band strengths in SaSt 2-3 and Tc 1 are the strongest amongst all the fullerene-containing objects.

[★] Based on observations made with NAOJ Subaru Telescope under the programme IDs: S13B-188S and S16A-227S (PI of both programme is M. Otsuka) and made with NOAO/WIYN telescope (programme ID: 2013A-0429, PI: M. Meixner)

[†] E-mail: otsuka@kustastro.kyoto-u.ac.jp

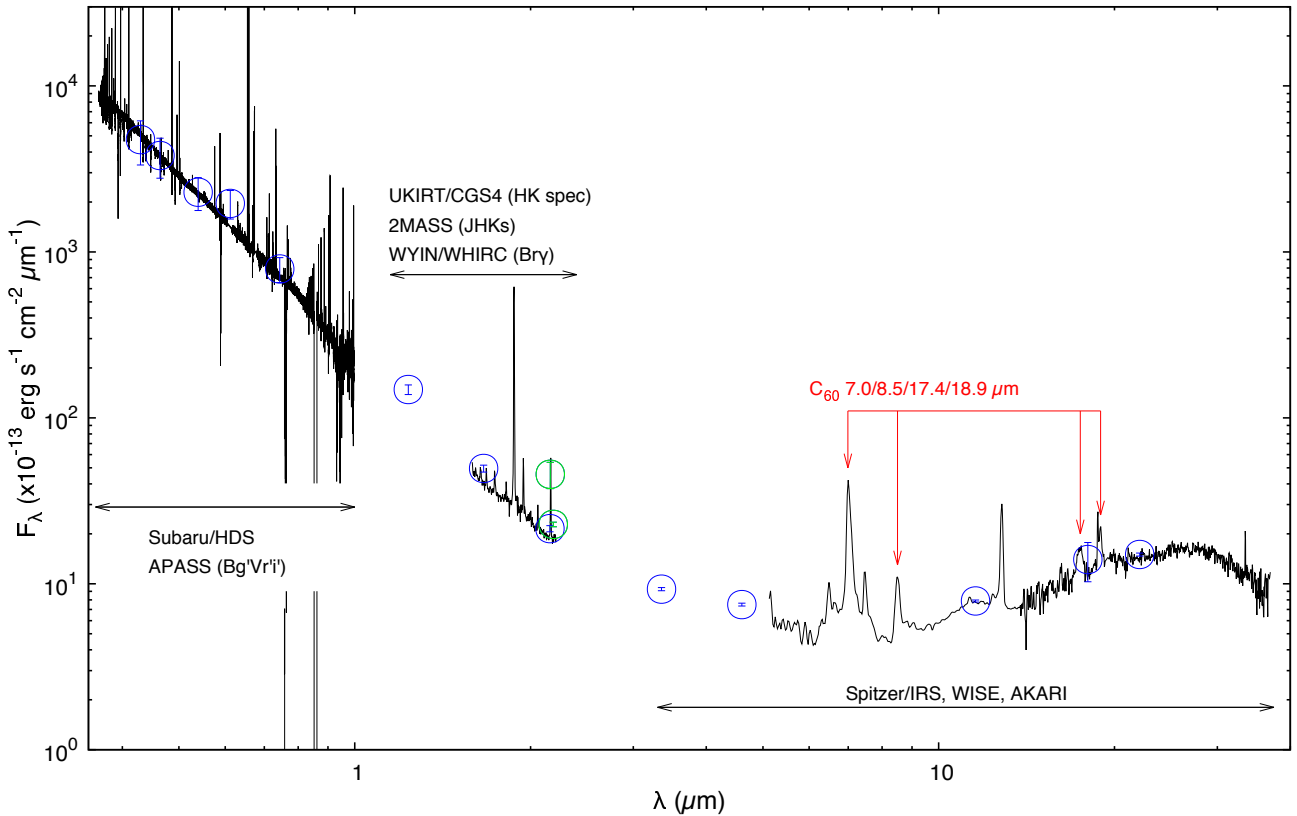


Figure 1. Panchromatic data of SaSt 2-3 used in the present work. The green (WHIRC Bry-on/off bands) and blue circles (the other bands) are the photometry data and the black lines are the spectra, respectively. The flux density of the Subaru/HDS spectrum is scaled to match the APASS $Bg'Vr'i'$ -bands. The UKIRT 3.8 m/Cooled Grating Spectrometer 4 (CGS4) HK -band spectrum (we downloaded the raw data of the spectrum presented in [Lumsden et al. \(2001\)](#) from the UKIRT archive data website and reduced them using IRAF) is scaled to match the 2MASS Ks -band. The *Spitzer*/IRS spectrum is scaled to match the *WISE*/W3 and W4 and *AKARI* L18W bands.

This strongly indicates that the fullerene formation in these two PNe is particularly efficient. Tc 1 has been extensively studied since the discovery of C_{60} . However, SaSt 2-3 is not entirely understood due to the lack of available data for the central star and nebula and its uncertain distance (D). The uncertain D towards SaSt 2-3 has led to different estimates of the central star luminosity (L_*) and effective temperature (T_{eff}); accordingly, this has led to inconsistencies in understanding the evolutionary status of this PN ([Gesicki & Zijlstra 2007](#); [Otsuka et al. 2014](#)). What we know from the prior studies is that this object has low-metallicity ($\epsilon(S) = 5.48^3$, [Pereira & Miranda 2007](#)) and is (possibly) a Type IV PN (i.e. halo population, [Pereira & Miranda 2007](#)).

If we obtain the UV to optical wavelength spectra of the central star as well as the nebula, we can resolve issues raised and verify conclusions from previous studies of SaSt 2-3; by so doing, we can hope to gain insights into the C_{60} formation. Fortunately, the UV-optical photometry data from the AAVSO Photometric All Sky Survey (APASS, [Henden et al. 2016](#)) can rigorously constrain L_* , and [Frew et al. \(2016\)](#) improved its distance estimate ($D = 14.86 \pm 4.26$ kpc). Therefore, we perform a comprehensive analysis on our own high-dispersion spectra of SaSt 2-3 taken using the 8.2 m Subaru telescope/high dispersion spectrograph (HDS, [Noguchi et al. 2002](#)) and archived multiwavelength data.

We organise the next sections as follows. In § 2, we describe our HDS spectroscopy and near-IR imaging using the NOAO WIYN 3.5 m/WIYN High-Resolution Infrared Camera (WHIRC, [Meixner et al. 2010](#)) and the reduction of this data. The *Spitzer*/IRS observation and its data reduction are described in [Otsuka et al. \(2014\)](#). In Fig. 1, we plot all the data used in the present work. In § 3, we perform plasma-diagnostics and derive ionic/elemental abundances. In § 4, we derive photospheric elemental abundances, T_{eff} , and surface gravity $\log g$ by fitting the stellar absorption using the theoretical stellar atmosphere code TLUSTY ([Hubeny 1988](#)). In § 5, we compare the derived nebular and stellar elemental abundances with those values predicted by AGB nucleosynthesis models in order to infer the initial mass of the progenitor star. In § 6, we build the spectral energy distribution (SED) model using the photoionisation code Cloudy (v.13.05, [Ferland et al. 2013](#)) to be consistent with all the derived quantities based on our determined D . In § 7, we discuss the origin and evolution of SaSt 2-3 and the C_{60} formation in PNe by comparison of the derived nebular/stellar properties with other non- C_{60} and C_{60} -containing PNe. Finally, we summarise the present work.

³ $\epsilon(X)$ equals to $12 + \log_{10} n(X)/n(H)$, where X is the target element and $n(X)/n(H)$ is the number density ratio relative to hydrogen.

2 DATA SET AND REDUCTION

2.1 Subaru/HDS observation

We secured high-dispersion echelle spectra using the HDS located at one of the Nasmyth loci of the 8.2 m Subaru Telescope at the top of Mauna Kea in Hawai'i. We summarise our observations in Table 1. We selected the 2×2 on-chip binning pattern. We set the slit-width to be $1.2''$. We used the blue cross disperser for the $3640 - 5390 \text{ \AA}$ observation and the red one for the $4740 - 7490 \text{ \AA}$ and $7190 - 9960 \text{ \AA}$ observations, respectively. We utilised the atmospheric dispersion corrector (ADC) during the observations. In all the observations, we observed the standard star Hiltner 600 for correcting echelle blaze functions and flux density simultaneously. In the $7190 - 9960 \text{ \AA}$ observation, we observed the telluric standard stars HD 61017 (B9III, $m_V = 6.68$) and HD 62217 (B9V, $m_V = 8.26$) at similar airmass.

We reduced the data using IRAF⁴ in a standard manner, including over-scan subtraction, scattered light subtraction between echelle orders, and telluric absorption removal. We adopted the atmospheric extinction correction function measured by Buton et al. (2013) at Mauna Kea. We measured the actual spectral resolution ($R = \lambda/\delta\lambda = 32\,300 - 33\,500$, see Table 1) using >300 Th-Ar comparison lines. The signal-to-noise ratio (S/N) for continuum reaches ~ 40 at $\sim 3640 \text{ \AA}$ and ~ 11 at $\sim 9950 \text{ \AA}$. In $\sim 3700 - 4800 \text{ \AA}$ (this range is important in stellar absorption fittings), S/N is >70 . We scaled both spectra to the average flux density in the overlapping regions ($4740 - 5390 \text{ \AA}$ and $7190 - 7490 \text{ \AA}$), and we connected these scaled spectra into a single $3640 - 9960 \text{ \AA}$ spectrum. The resultant spectrum is presented in Fig. 1.

2.2 Flux measurements and interstellar extinction correction

We measure emission line fluxes by multiple Gaussian component fitting. Then, we correct these observed fluxes $F(\lambda)$ to obtain the interstellar extinction corrected fluxes $I(\lambda)$ using the following formula;

$$I(\lambda) = F(\lambda) \cdot 10^{c(\text{H}\beta)(1+f(\lambda))}, \quad (1)$$

where $f(\lambda)$ is the interstellar extinction function at λ computed by the reddening law of Cardelli et al. (1989). To verify R_V accurately, $\sim 2000 - 2500 \text{ \AA}$ spectra/photometry data would be necessary because $f(\lambda)$ and R_V are sensitive to this wavelength range. At the moment, there are no available spectra/photometry data in such wavelength range. Therefore, we adopt an average $R_V = 3.1$ in the Milky Way. Applying $R_V = 3.1$ to SaSt 2-3 seems to be acceptable because Wegner (2003) reported $R_V = 3.64 \pm 0.43$ towards HD 60855 (B2Ve). HD 60855 is a star in the direction closer to SaSt 2-3 amongst stars whose R_V has been measured. $c(\text{H}\beta)$ is the reddening coefficient at $\text{H}\beta$, corresponding to $\log_{10} I(\text{H}\beta)/F(\text{H}\beta)$.

We determine $c(\text{H}\beta)$ values by comparing the observed Balmer and Paschen line ratios to $\text{H}\beta$ with the theoretical ratios of Storey & Hummer (1995) for the case with an electron temperature $T_e = 10^4 \text{ K}$ and an electron density $n_e = 2000 \text{ cm}^{-3}$ under the Case B assumption. We calculate this n_e using the $[\text{O II}] F(3726 \text{ \AA})/F(3729 \text{ \AA})$ and the $[\text{Cl III}] F(5517 \text{ \AA})/F(5537 \text{ \AA})$ ratios.

⁴ IRAF is distributed by the National Optical Astronomy Observatories, operated by the Association of Universities for Research in Astronomy (AURA), Inc., under a cooperative agreement with the National Science Foundation.

Table 1. HDS and WHIRC observation log for SaSt 2-3.

Date	λ (\AA)	$\lambda/\delta\lambda$ (ave.)	Exp. time	Condition/Seeing
2013/10/06	3640 – 5390	33 500	$2 \times 200 \text{ s}$, 2600 s	thin cloud, $\sim 0.7''$
2013/12/10	4740 – 7490	33 300	100, 500, 900 s	clear, $\sim 0.7''$
2016/02/01	7190 – 9960	32 300	180 s, $4 \times 1600 \text{ s}$	clear, $\sim 0.7\text{-}1.0''$
Date	Band	Pixel scale	Exp. time	Condition/Seeing
2013/04/24	Br γ , Br $\gamma 45$	$0.1'' \times 0.1''$	$5 \text{ pts} \times 120 \text{ s}$	clear, $\sim 0.6\text{-}0.7''$

For the $3640 - 5390 \text{ \AA}$ spectrum, we obtain $c(\text{H}\beta) = 0.20 \pm 0.01$, which is the intensity-weight average amongst the $\text{H}\gamma$, $\text{H}\delta$, $\text{H}\epsilon$, and $\text{H}\eta$ to the $\text{H}\beta$ ratios. For the $4740 - 7490 \text{ \AA}$ spectrum, we obtain $c(\text{H}\beta) = 0.40 \pm 0.01$ from the $\text{H}\alpha/\text{H}\beta$ ratio. For the $7190 - 9960 \text{ \AA}$ spectrum, we determine $c(\text{H}\beta) = 0.24 \pm 0.03$ from the Paschen $\text{H} 19014 \text{ \AA}$ (P10) to the $\text{H}\beta$ ratio. For all HDS spectra, we adopt the average $c(\text{H}\beta) = 0.28 \pm 0.11$ amongst three HDS observations.

Tylenda et al. (1992) reported $c(\text{H}\beta) = 1.11$ (observation date is unknown). We derive the average $c(\text{H}\beta) = 1.11 \pm 0.26$ using the ratio of $F(\text{H}\alpha)$, $F(\text{H}\gamma)$, and $F(\text{H}\delta)$ to $F(\text{H}\beta)$ measured from their spectrum⁵. Based on the $F(\text{H}\alpha)$ and $F(\text{H}\beta)$ reported by Dopita & Hua (1997), we obtain $c(\text{H}\beta) = 0.43 \pm 0.04$ (obs date: 1997 March). Pereira & Miranda (2007) reported $E(B - V) = 0.11 \pm 0.02$, which corresponds to $c(\text{H}\beta) = 0.13 - 0.19$ (obs date: 2005 Feb). Using the line flux table of Pereira & Miranda (2007), we obtain the average $c(\text{H}\beta) = 0.41 \pm 0.23$ calculated from $F(\text{H}\alpha)$, $F(\text{H}\gamma)$, and $F(\text{P}10)$ to $F(\text{H}\beta)$. Using the archived ESO Faint Object Spectrograph and Camera (EFOSC) spectrum taken on 2000 April⁶, we obtain a $c(\text{H}\beta) = 0.68 \pm 0.11$ measured from the $F(\text{H}\alpha)/F(\text{H}\beta)$ ratio. A time variation of $c(\text{H}\beta)$ seen between 1992 and 2016 might be due to affect of stellar H I absorption to corresponding nebular H I and also orbital motion of the binary central star (§ 4.2).

We scale the *Spitzer*/IRS spectrum to match the Wide-field Infrared Survey Explorer (*WISE*) W3/W4 band flux densities of Cutri (2014) and the L18W *AKARI*/IRC mid-infrared all-sky survey of Ishihara et al. (2010) (see § 2.4). For this scaled *Spitzer*/IRS spectrum, we do not correct interstellar extinction because the interstellar extinction is negligibly small in the mid-IR wavelength. It is common practice in nebular analyses to scale all line intensities in such a way that $\text{H}\beta$ has a line flux of 100. To achieve this, we first normalise the line fluxes with respect the complex of the $\text{H} 17.46 \mu\text{m}$ ($n = 5 - 6$, n is the quantum number) and $7.50 \mu\text{m}$ ($n = 6 - 8$) lines. $F(7.48/7.50 \mu\text{m})$ is $(4.87 \pm 0.30) \times 10^{-15} \text{ erg s}^{-1} \text{ cm}^{-2}$ ($A(-B)$ means $A \times 10^{-B}$ hereafter). According to Storey & Hummer (1995) for the Case B assumption with $T_e = 10^4 \text{ K}$ and $n_e = 2000 \text{ cm}^{-3}$, the ratio of $\text{H} 17.48/7.50 \mu\text{m}/I(\text{H}\beta) = 3.102/100$. Finally, we multiply all the normalised line fluxes by 3.102 to express them relative to $\text{H}\beta$ with $I(\text{H}\beta) = 100$.

In Appendix Table A1, we list the identified emission lines in the Subaru/HDS and *Spitzer*/IRS spectra. The first column is the laboratory wavelength in air. Here, $I(\text{H}\beta)$ is 100. The last column $\delta I(\lambda)$ corresponds to $1-\sigma$.

2.3 NOAO/WHIRC near-IR imaging observation

We took the high-resolution images using NOAO WIYN 3.5 m/WHIRC. We summarise the observation log in Table 1. We took

⁵ We downloaded this spectrum from HASH PN database. <http://202.189.117.101:8999/gpne/index.php>.

⁶ The spectrum was taken by Acker et al (Programme ID: 64.H-0279(A)).

the two narrowband images using the Br γ ($\lambda_c = 2.162 \mu\text{m}$, effective band width ($W_{\text{eff}} = 0.210 \mu\text{m}$) and Br $\gamma 45$ ($\lambda_c = 2.188 \mu\text{m}$, $W_{\text{eff}} = 0.245 \mu\text{m}$) filters⁷. We selected a 5 pts dithering pattern. We followed a standard manner for near-IR imaging data reductions using IRAF, including background sky and dark current subtraction, bad pixel masking, flat-fielding, and distortion correction. Finally, we obtained a single averaged image for each band.

For the flux calibration, we utilised the SED of the standard star 2MASS07480394-1407155 based on its photometry between the two micron all sky survey (2MASS, *Cutri et al. 2003*) *JHKs* and *WISE* bands W1/W2. The SED of this star can be well fitted with a single blackbody temperature of 3510 K. Then, we derived the flux density in each band by taking each filter transmission curve into account. Next, we measured the respective count of the standard star in the Br γ and Br $\gamma 45$ images. Thus, we obtained the conversion factor from the counts in ADU to flux density in $\text{erg s}^{-1} \text{cm}^{-2} \mu\text{m}^{-1}$. The measured flux density in each band is listed in Appendix Table A2 and plotted in Fig. 1 (green circles).

2.4 Photometry data

To support the present work, we collected the data taken from APASS, 2MASS, *WISE*, and *AKARI*/Infrared Camera (IRC). In Table A2, we list the observed and reddening corrected flux densities F_λ and I_λ , respectively. We obtain I_λ using Equation (1) and the average $c(\text{H}\beta) = 0.28 \pm 0.11$ amongst three HDS observations (§ 2.2). Due to negligibly small reddening effect, we do not correct F_λ in the longer wavelength than *WISE* W1 band ($3.35 \mu\text{m}$).

3 NEBULAR LINE ANALYSIS

3.1 Systemic nebular radial velocity

We obtain the average heliocentric radial velocity of $+166.6 \text{ km s}^{-1}$ measured from the identified 128 nebular lines in the HDS spectrum (the standard deviation is 3.2 km s^{-1} amongst all these lines and that of each radial velocity is 0.52 km s^{-1} in the average). The LSR radial velocity $v_r(\text{LSR})$ of $+149.1 \text{ km s}^{-1}$ is much faster than $v_r(\text{LSR})$ in other Galactic PNe toward $l \sim 220 - 240^\circ$ and $b \lesssim \pm 10^\circ$ ($\lesssim +80 \text{ km s}^{-1}$; *Quiroza et al. 2007*). $v_r(\text{LSR})$ of $+105 \text{ km s}^{-1}$ in the C₆₀ PN M1-9 (PN G214.0+04.3, *Otsuka et al. 2014*) is the closest to SaSt 2-3's $v_r(\text{LSR})$ (*Quiroza et al. 2007*). Peculiar velocity relative to Galactic rotation is calculated using $v_r(\text{LSR})$ and D in order to classify PNe into Type I-IV (i.e., thin/thick disc and halo; see e.g., *Peimbert 1978*). We discuss classification of SaSt 2-3 in § 7.1. We do not find a time-variation of the radial velocity measured by the nebular lines. We report the radial velocity measurements from the stellar absorption in § 4.2.

3.2 H β flux of the entire nebula

From the measured $F(\text{H}17.48/7.50 \mu\text{m})$ and the theoretical $I(\text{H}17.48/7.50 \mu\text{m})/I(\text{H}\beta)$ ratio = 3.102/100 (see § 2.2), we obtain $I(\text{H}\beta)$ of the entire nebula to be $(1.57 \pm 0.28)(-12) \text{ erg s}^{-1} \text{cm}^{-2}$. $F(\text{H}\alpha)$ and $F(\text{H}\beta)$ using the $5''$ wide slit observation by *Dopita & Hua (1997)* and $c(\text{H}\beta) = 0.43 \pm 0.04$ (§ 2.2) yields $I(\text{H}\beta) = (1.97 \pm 0.20)(-12) \text{ erg s}^{-1} \text{cm}^{-2}$, which is consistent with ours. In the present work, we adopt our own calculated $I(\text{H}\beta)$ for the

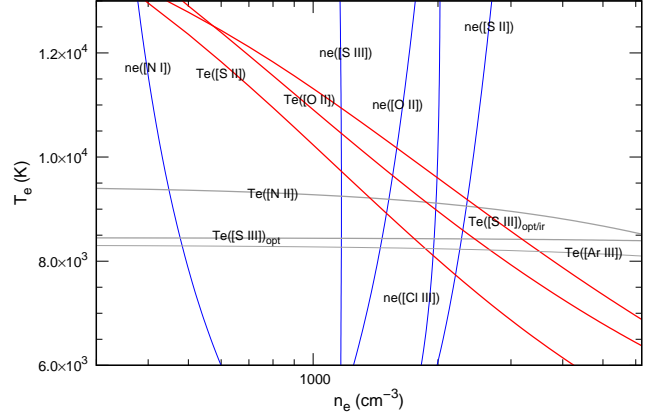


Figure 2. $n_e - T_e$ diagram of SaSt 2-3. n_e , T_e , and both n_e and T_e diagnostic curves are indicated by the blue, grey, and red lines, respectively. $T_e([\text{S III}]_{\text{opt}})$ and $T_e([\text{S III}]_{\text{opt/ir}})$ curves are the results by the $[\text{S III}] I(9069 \text{ \AA})/I(6313 \text{ \AA})$ and $[\text{S III}] I(9069 \text{ \AA})/I(18.71/33.47 \mu\text{m})$ ratios, respectively. See also Table 2.

Table 2. Summary of plasma diagnostics. Since the lower limit $[\text{N I}] I(5198 \text{ \AA})/I(5200 \text{ \AA})$ ratio is out of the range of the $n_e([\text{N I}])$ derivation, we give the upper limit $n_e([\text{N I}]) = 1460 \text{ cm}^{-3}$.

CEL n_e -diagnostic line ratio	Ratio	Result (cm^{-3})
$[\text{N I}] I(5198 \text{ \AA})/I(5200 \text{ \AA})$	1.088 ± 0.498	460
$[\text{S II}] I(6717 \text{ \AA})/I(6731 \text{ \AA})$	0.663 ± 0.074	2680 ± 1070
$[\text{O II}] I(3726 \text{ \AA})/I(3729 \text{ \AA})$	1.440 ± 0.163	1560 ± 490
$[\text{Cl III}] I(5517 \text{ \AA})/I(5537 \text{ \AA})$	1.048 ± 0.130	2180 ± 1070
$[\text{S III}] I(18.71 \mu\text{m})/I(33.47 \mu\text{m})$	1.314 ± 0.334	1190 ± 570
CEL T_e -diagnostic line ratio	Ratio	Result (K)
$[\text{N II}] I(6548/83 \text{ \AA})/I(5755 \text{ \AA})$	114.881 ± 8.621	9200 ± 260
$[\text{S III}] I(9069 \text{ \AA})/I(6313 \text{ \AA})$	14.443 ± 2.558	8530 ± 570
$[\text{Ar III}] I(7135/7751 \text{ \AA})/I(8.99 \mu\text{m})$	0.952 ± 0.197	8250 ± 790
CEL n_e & T_e -diagnostic line ratio	Ratio	Result (K)
$[\text{S II}] I(6717/31 \text{ \AA})/I(4069 \text{ \AA})$	10.322 ± 0.958	7220 ± 430
$[\text{O II}] I(3726/3729 \text{ \AA})/I(7320/30 \text{ \AA})$	26.725 ± 2.103	9670 ± 430
$[\text{S III}] I(9069 \text{ \AA})/I(18.71/33.47 \mu\text{m})$	0.278 ± 0.054	$11\,040 \pm 1860$
RL T_e -diagnostic line ratio	Ratio	Result (K)
$I_\lambda(8194 \text{ \AA}) - I_\lambda(8169 \text{ \AA})/I(\text{P}11)$	0.022 ± 0.004	7340 ± 2610
$\text{He I}(7281 \text{ \AA})/I(6678 \text{ \AA})$	0.256 ± 0.036	$11\,830 \pm 1790$

entire nebula because our $I(\text{H}\beta)$ is based on interstellar extinction free and stellar H I absorption effect less mid-IR H I $7.48/7.50 \mu\text{m}$.

3.3 Plasma diagnostics

We determine n_e and T_e using diagnostic line ratios listed in Table 2, with the resulting $n_e - T_e$ diagnostic curves for the collisionally excited lines (CELs) shown in Fig. 2. The roughly vertical (blue) lines can be used to determine n_e ; more horizontal (grey) lines T_e . Although the other diagnostic curves (red) yield both n_e and T_e , we use them as T_e indicators here. Since the emission of each ion originates from regions of different T_e and n_e , we need to determine both parameters for each ion independently so that we can determine accurate ionic abundances later on. This involves several steps. First, we note that $T_e \sim 9000 \text{ K}$ from $T_e([\text{Ar III}])$, $T_e([\text{S III}]_{\text{opt}})$, and $T_e([\text{N II}])$ curves. Next, we adopt $T_e = 9000 \text{ K}$ to solve each equation of population at ≥ 5 multiple energy levels for each n_e sensitive ions; from this, we then calculate n_e from the corresponding diagnostic line ratios for $[\text{N I}]$, $[\text{S II}]$, $[\text{O II}]$, $[\text{Cl III}]$, and $[\text{S III}]$ (see Table 2). Note that the precise T_e we assume here does not

⁷ <https://www.noao.edu/kpno/manuals/whirc/filters.html>

Table 3. Adopting T_e and n_e for the CEL ionic abundance calculations.

Ion	T_e (K)	n_e (cm^{-3})
$\text{N}^0, \text{O}^0, \text{S}^+$	$T_e([\text{S II}])$	$n_e([\text{S II}])$
N^+	$T_e([\text{N II}])$	$n_e([\text{N II}])$
O^+	$T_e([\text{O II}])$	$n_e([\text{O II}])$
$\text{O}^{2+}, \text{Ne}^+$	9270 ± 1070	1690 ± 820
S^{2+}	9790 ± 1220	$n_e([\text{S III}])$
Ar^{2+}	$T_e([\text{Ar III}])$	1690 ± 820
$\text{Cl}^+, \text{Fe}^{2+}$	9440 ± 350	$n_e([\text{O II}])$
Cl^{2+}	9270 ± 1070	$n_e([\text{Cl III}])$

matter much, since these n_e diagnostic line ratios are fairly insensitive to T_e . With the n_e values established, we then determine T_e by adopting the derived n_e values corresponding to each ion. We adopt $n_e([\text{O II}])$ for $T_e([\text{N II}])$ derivation. Our derived values are in agreement with those by [Pereira & Miranda \(2007\)](#) who found $n_e([\text{S II}]) = 2100 \pm 600 \text{ cm}^{-3}$ and $T_e([\text{N II}]) = 9600 \pm 930 \text{ K}$.

We compute $T_e(\text{He I})$ using singlet He I lines. To calculate $T_e(\text{PJ})$ from the Paschen continuum discontinuity by utilising the equation (7) of [Fang & Liu \(2011\)](#), first we determine the He^+ abundance of $1.09(-2) \pm 2.28(-4)$ under the obtained $T_e(\text{He I})$. Eventually, we utilise $T_e(\text{He I})$ for both He^+ and C^{2+} abundance calculations due to higher $T_e(\text{PJ})$ uncertainty.

3.4 Ionic abundance derivations

We calculate the CEL ionic abundances by solving an equation of population at multiple energy levels under the adopted T_e and n_e as listed in Table 3; $T_e = 9270 \text{ K}$ is the average value amongst two $T_e([\text{S III}])$ and $T_e([\text{Ar III}])$, $T_e = 9790 \text{ K}$ is the average value amongst two $T_e([\text{S III}])$, $T_e = 9440 \text{ K}$ is the average between $T_e([\text{N II}])$ and $T_e([\text{O II}])$, and $n_e = 1690 \text{ cm}^{-3}$ is the average between $n_e([\text{Cl III}])$ and $n_e([\text{S III}])$. For the recombination line (RL) He^+ and C^{2+} , we adopt $T_e(\text{He I})$ and $n_e = 10^4 \text{ cm}^{-3}$. Our choice of the T_e - n_e pair of each ion depends on the potential (IP) of the targeting ion. Except for the CEL N^+ , O^{+2+} , and S^+ which [Pereira & Miranda \(2007\)](#) already measured, the first measurements of all the ionic abundances are done by us. We summarise the resultant CEL and RL ionic abundances in Appendix Table A3. We calculate each ionic abundance using each line intensity. Then, we adopt the weight-average value as the representative ionic abundance as listed in the last line of each ion. We give $1\text{-}\sigma$ uncertainty of each ionic abundance, which accounts for the uncertainties of line fluxes (including $c(\text{H}\beta)$ uncertainty), T_e , and n_e .

The He^+ abundance of $9.72(-3)$ in SaSt2-3 is ten times smaller than in evolved PNe (e.g., $T_{\text{eff}} \gtrsim 50\,000 \text{ K}$). For instance, in the C_{60} PN M 1-20 ($T_{\text{eff}} = 45\,880 \text{ K}$, [Otsuka et al. 2014](#)), [Wang & Liu \(2007\)](#) find He^+ abundance of $9.50(-2)$. Moreover, the He^+ abundance is also significantly lower than in other Galactic C_{60} PNe with $T_{\text{eff}} \lesssim 40\,000 \text{ K}$ where He^+ abundances have been determined: $6.99(-2)$ in IC 418 ([Hyung et al. 1994](#)), $6.57(-2)$ in M 1-6 ([Otsuka in prep](#)), $3.93(-2)$ in M 1-11 ([Otsuka et al. 2013](#)), $3.5(-2)$ in M 1-12 ([Henry et al. 2010](#)), and $6.0(-2)$ in Tc 1 ([Pottasch et al. 2011](#)). Similar to the C_{60} PN Lin 49 in the SMC ([Otsuka et al. 2016](#)), the low He^+ abundance is due to the smaller number of ionising photons for He^+ ($\geq 21 \text{ eV}$): using the spectra synthesised by TLUSTY (with $L_* = 7000 L_\odot$, $\log g = 3.11 \text{ cm s}^{-2}$, metallicity $Z = 1/10 Z_\odot$, see below), we estimate the number of photon with energy $\geq 21 \text{ eV}$ to be $8.3(+45) \text{ s}^{-1}$ in a $T_{\text{eff}} = 28\,100 \text{ K}$ star like SaSt2-3 (see § 4) and $4.8(+46) \text{ s}^{-1}$ in $T_{\text{eff}} = 32\,000 \text{ K}$ stars like M 1-11 and M 1-12.

Table 4. Nebular elemental abundances using the ICFs. The last column (PM07) is the $\epsilon(X)$ value derived by [Pereira & Miranda \(2007\)](#).

X	$n(X)/n(\text{H})$ (Ours)	$\epsilon(X)$ (Ours)	$\epsilon(X) - \epsilon(X_\odot)$ (Ours)	$\epsilon(X)$ (PM07)
He	$5.58(-2) - 1.26(-1)$	$10.75 - 11.10$	$-0.15 - +0.20$...
C	$1.61(-3) \pm 4.61(-4)$	9.21 ± 0.12	$+0.82 \pm 0.13$...
N	$2.95(-5) \pm 4.09(-6)$	7.47 ± 0.06	-0.36 ± 0.13	7.38 ± 0.14
O	$1.30(-4) \pm 1.10(-5)$	8.11 ± 0.04	-0.58 ± 0.06	8.27 ± 0.14
Ne	$2.91(-5) \pm 2.85(-6)$	7.46 ± 0.04	-0.41 ± 0.11	...
S	$1.26(-6) \pm 8.80(-8)$	6.10 ± 0.03	-1.09 ± 0.05	5.48 ± 0.14
Cl	$3.68(-8) \pm 5.51(-9)$	4.57 ± 0.07	-0.69 ± 0.09	...
Ar	$4.62(-7) \pm 1.43(-7)$	5.66 ± 0.13	-0.89 ± 0.16	...
Fe	$1.94(-7) \pm 2.74(-8)$	5.29 ± 0.06	-2.18 ± 0.07	...

Thus, the majority of the He atoms in SaSt2-3 are in the neutral state.

The higher multiplet C II lines are generally reliable because these lines are less affected by resonance fluorescence. However, the higher C^{2+} abundances from the C II 3918.98/20.69 Å ($4s^2S - 3p^2P$) and 7231.32/36.42 Å ($3d^2D - 3p^2P$) are likely due to the enhancement by resonance from the 635.25/636.99 Å ($4s^2S - 2p^2P$) and the 687 Å ($3d^2D - 2p^2P$), respectively. Thus, we exclude the C^{2+} abundances from these C II lines and C II 6451.95 Å⁸ in the representative RL C^{2+} determination.

Our N^+ and O^{+2+} are comparable with [Pereira & Miranda \(2007\)](#), who calculated $\text{N}^+ = 2.42(-5)$, $\text{O}^+ = 1.87(-4)$, $\text{O}^{2+} = 1.22(-6)$, and $\text{S}^+ = 3.0(-7)$ (they note that their derived ionic abundances has $\pm 30\%$ uncertainty) under $T_e([\text{N II}]) = 9600 \text{ K}$ and $n_e([\text{S II}]) = 2100 \text{ cm}^{-3}$. The discrepancy between their and our S^+ ($5.89(-7)$) is caused by T_e selection; if we adopt $T_e = 9600 \text{ K}$ and $n_e = 2100 \text{ cm}^{-3}$, we obtain $\text{S}^+ = 3.48(-7)$.

3.5 Elemental abundance derivations using the ICFs

To obtain the elemental abundances using the derived ionic abundances, we introduce the ionisation correction factors (ICFs, see e.g., [Delgado-Inglada et al. 2014](#), for details). Here, the number density ratio of the element X with respect to the hydrogen, $n(X)/n(\text{H})$ is equal to $\text{ICF}(X) \cdot \sum_{m=1} n(X^{m+})/n(\text{H}^+)$. The ICFs have been empirically determined based on the fraction of observed ion number densities with similar ionisation potentials to the target element, and have also been determined based on the fractions of the ions calculated by photoionisation models. Since SaSt2-3 is very low-excitation PN, the ICFs (He in particular) adopted for more highly excited PNe do not work well. Therefore, we need a special treatment for SaSt2-3. Thus, in addition to the ICFs established by photoionisation grid models of [Delgado-Inglada et al. \(2014\)](#), we refer to ICFs in Lin 49 by [Otsuka et al. \(2016\)](#).

In Lin 49, the C^{2+}/C ratio is similar to the Ar^{2+}/Ar ratio. For SaSt2-3, we adopt equation (A6) of [Otsuka et al. \(2016\)](#) for C and Ar. Both $\text{ICF}(\text{C})$ and $\text{ICF}(\text{Ar})$ are $2.7 \cdot (\text{Cl}/\text{Cl}^{2+}) = 5.12 \pm 1.41$. For He derivation, we adopt two $\text{ICF}(\text{He})$ calculated using the equation (42) of [Peimbert & Costero \(1969, 11.57\) and from the ratio of \$\text{Ar}/\text{Ar}^{2+}\$ \(5.12\). \$\text{ICF}\(\text{N}\) = 1.04 \pm 0.13\$ is from \[Delgado-Inglada et al. \\(2014\\)\]\(#\). \$\text{ICF}\(\text{Fe}\) = 1.31 \pm 0.16\$ is from \[Delgado-Inglada & Rodríguez \\(2014\\)\]\(#\) based on the observation results. ICF of the other elements is unity. We verify whether the](#)

⁸ Because the C^{2+} abundance from this line is about three time larger than that from the C II 4267 Å. The C II 4267 Å is the most reliable RL C^{2+} indicator.

adopted ICFs here are proper by comparing with CLOUDY photoionisation model (§ 6).

In the second and third columns of Table 4, we present the resultant elemental abundances with 1- σ uncertainty, except for $\epsilon(\text{He})$, where we adopt its range. The two columns are the relative abundance to the solar value by Lodders (2010) and the $\epsilon(\text{X})$ by Pereira & Miranda (2007). Our $\epsilon(\text{N})$ and $\epsilon(\text{O})$ are consistent with Pereira & Miranda (2007). As explained in § 3.4, $\epsilon(\text{S})$ discrepancy between theirs and ours is attributed to the S^+ abundance. By the CLOUDY model under $D = 6$ kpc, Otsuka et al. (2014) derived $\epsilon(\text{N/O/Ne/S/Ar}) = 7.49, 8.23, 7.68, 6.17,$ and 5.93 based on the optical spectrum of Pereira & Miranda (2007) and the *Spitzer*/IRS spectrum. Otsuka et al. (2014) estimated an expected CEL $\epsilon(\text{C}) = 8.72$ using a $[\text{C}/\text{H}] - [\text{C}/\text{Ar}]$ relation established amongst 115 Galactic PNe. Delgado-Inglada & Rodríguez (2014) reported that the RL C^{2+} to the CEL C^{2+} ratio in IC 418 is 2.4. Applying this value to SaSt 2-3, we obtain an expected CEL $\epsilon(\text{C}) = 8.83 \pm 0.12$, which is consistent with Otsuka et al. (2014). We attempt to obtain more plausible expected CEL $\epsilon(\text{C})$ using the stellar $\epsilon(\text{C})$ and $\epsilon(\text{O})$ in § 4.1. The $[\text{Ne}/\text{H}]$ is comparable with the $[\text{O}/\text{H}]$ because Ne together with O had been synthesised in the He-rich intershell during the AGB phase. The Ne enhancement would be due to the increase of ^{22}Ne .

The $[\text{S}, \text{Cl}, \text{Ar}/\text{H}]$ abundances are low, and if these represent the stellar abundances, then SaSt 2-3 is the lowest metallicity object amongst the Galactic C_{60} PNe, and we infer $Z \sim 0.1 Z_{\odot}$ from the average $[\text{S}, \text{Cl}, \text{Ar}/\text{H}]$. While most Ar is probably in the gas phase in this object, S could be incorporated into dust grains (e.g. MgS , suggested to be a candidate for the carrier of the broad $30\mu\text{m}$ feature that is observed in the C_{60} PNe). Fe is even more depleted, but it is unlikely that this represents the initial abundance given the other elemental abundances. Rather, a fraction of the Fe will be incorporated into dust grains. We discuss further the elemental abundances in § 5.

4 STELLAR ABSORPTION ANALYSIS

4.1 Stellar parameter derivations

We perform stellar absorption analysis of the HDS spectra taken on 2013 Oct 6 and Dec 10 using the non-local thermodynamic equilibrium (non-LTE) stellar atmosphere modelling code TLUSTY. We detect strong Si III,IV and He II absorption lines. From our TLUSTY modelling, T_{eff} of the central star is 28 100 K (Table 5), which is cooler than $T_{\text{eff}} \geq 30\,000$ K in the O-type stars. Thus, we classify the stellar spectrum of SaSt 2-3 into early B-type giant B0-III rather than O-type. Thus, we use comprehensive grid of 1540 metal line-blanketed, non-LTE, plane-parallel, hydrostatic model atmospheres of B-type stars BSTAR2006⁹ by Lanz & Hubeny (2007).

We find the average nebular $[\text{Cl}, \text{S}, \text{Ar}/\text{H}]$ of -0.89 ± 0.12 (§ 3.5). Assuming that the metallicity Z of the central star and the nebula is roughly the same as seen in the case of IC 418 by Morisset & Georgiev (2009), we adopt the $Z = 0.1 Z_{\odot}$ model grid from BSTAR2006. All of the *initial* abundances in this model grid are set to $\epsilon(\text{He}) = 11.00$ and $[\text{X}/\text{H}] = -1$ except for He. Based on the $Z = 0.1 Z_{\odot}$ model grid, we vary $\epsilon(\text{X})$ to yield each equivalent width (EW) of element X to compare with each $EW(\text{X})$ measured from the observed HDS spectra. Throughout our TLUSTY synthesis

Table 5. Summary of the set and derived parameters of the central star.

Parameter	Value	Parameter	Value
T_{eff} (K)	$28\,100 \pm 300$	$\epsilon(\text{He})$	10.99 ± 0.09
$\log g$ (cm s^{-2})	3.11 ± 0.05	$\epsilon(\text{C})$	8.56 ± 0.10
v_t (km s^{-1})	10 ± 2	$\epsilon(\text{N})$	7.26 ± 0.16
$v \sin(i)$ (km s^{-1})	56 ± 4	$\epsilon(\text{O})$	8.10 ± 0.17
		$\epsilon(\text{Si})$	6.81 ± 0.10

analysis, we do not set $[\text{He}, \text{C}, \text{N}, \text{O}, \text{Si}/\text{H}] = -1$ and we do not adopt the derived nebular $\text{He}, \text{C}, \text{N}, \text{O}/\text{H}$ as the stellar photospheric ones. Based on the measured EW of the identified 9 He I,II, 4 C III,IV, 2 N II,III, 13 O II, and 5 Si III,IV absorption, we derive the photospheric $\text{He}/\text{C}/\text{N}/\text{O}/\text{Si}$ abundances, microturbulent velocity (v_t), rotational velocity ($v \sin(i)$; i is the angle between the rotation axis and the line of sight), T_{eff} , and $\log g$ of the central star. These absorption lines are lesser affected by the nearby nebular lines and absorption lines of the other elements. As we report later, the central wavelength of the stellar absorption lines changes between observing dates whereas those of the nebular lines remain constant. Before analysis, we convert heliocentric wavelength frame of the HDS spectrum into rest frame using the radial velocity determined by the He II 4686 Å for the 2013 Oct 6 data ($154.8 \pm 2.3 \text{ km s}^{-1}$) and the He II 5411 Å for the 2013 Dec 10 data ($182.3 \pm 4.0 \text{ km s}^{-1}$).

First, we set the basic parameters characterising the stellar atmosphere, i.e., Z , v_t , T_{eff} , and $\log g$. By setting $T_{\text{eff}} = 28\,000$ K and $\log g = 3.10 \text{ cm s}^{-2}$, we investigate $\epsilon(\text{O})$ versus selected 8 O II lines' EW to determine v_t using SYNFIT. For each absorption, we set instrumental line broadening determined by measuring Th-Ar line widths. Since $v_t \geq 10 \text{ km s}^{-1}$ gives minimisation of the scatter in $\epsilon(\text{O})$ versus EW , we adopt $v_t = 10 \text{ km s}^{-1}$. As a reference, Morisset & Georgiev (2009) adopted $v_t = 10 \text{ km s}^{-1}$ for IC 418.

We determine T_{eff} and $\log g$ using the $T_{\text{eff}} - \log g$ curves generated by the model atmosphere with $v_t = 10 \text{ km s}^{-1}$, $Z = 0.1 Z_{\odot}$, and $\epsilon(\text{He}) = 10.90$. The $T_{\text{eff}} - \log g$ curves are generated by the following process; for a fixed T_{eff} , we vary $\log g$ from $2.90 - 3.30 \text{ cm s}^{-2}$ in a constant 0.01 cm s^{-2} step to find the best fit value for each observed He I,II's EW . We test the range of T_{eff} from $27\,500 - 28\,500$ K (200 K step).

Based on the determined v_t , T_{eff} , and $\log g$, we further constrain $\epsilon(\text{He})$ and calculate $\epsilon(\text{C}/\text{N}/\text{O}/\text{Si})$ abundances by comparing the observed and model predicted EW s of each line by SYNABUND¹⁰. We summarise the result in Table 5. In Appendix Table A4, we list the elemental abundances using each line. We adopt the average value as the representative abundance as listed in the last line of each element. The uncertainty of elemental abundances includes errors from the measured EW s, T_{eff} , $\log g$, and the uncertainty when we adopt the model atmosphere with the $[\text{Z}/\text{H}] = -0.90$ or -1.10 and when we assume the uncertainty of v_t of 2 km s^{-1} . We determine $v \sin(i)$ by line-profile fittings of the selected He I,II and H I in $4000 - 4700 \text{ Å}$ using SYNFIT¹¹.

In Fig. 3, we show the synthetic stellar spectrum generated using SYNOSPEC¹². We identify the absorption lines (except for H I) with the model predicted $EW \geq 10 \text{ mÅ}$ by the blue lines. The synthetic spectrum in $3700 - 4750 \text{ Å}$ is presented in Appendix Fig. A1. Stellar Ne, S, Ar, Mg, Ca, and Ti (α -elements) and Ni, Fe, and Zn

¹⁰ SYNABUND is a code developed by Prof. I. Hubeny in order to calculate EW s under TLUSTY stellar model atmosphere.

¹¹ SYNFIT is a code developed by Prof. I. Hubeny in order to synthesise line-profiles under TLUSTY stellar model atmosphere.

⁹ <http://tlusty.oca.eu/Tlusty2002/tlusty-frames-BS06.html> ¹² <http://nova.astro.umd.edu/Synspec49/synspec.html>

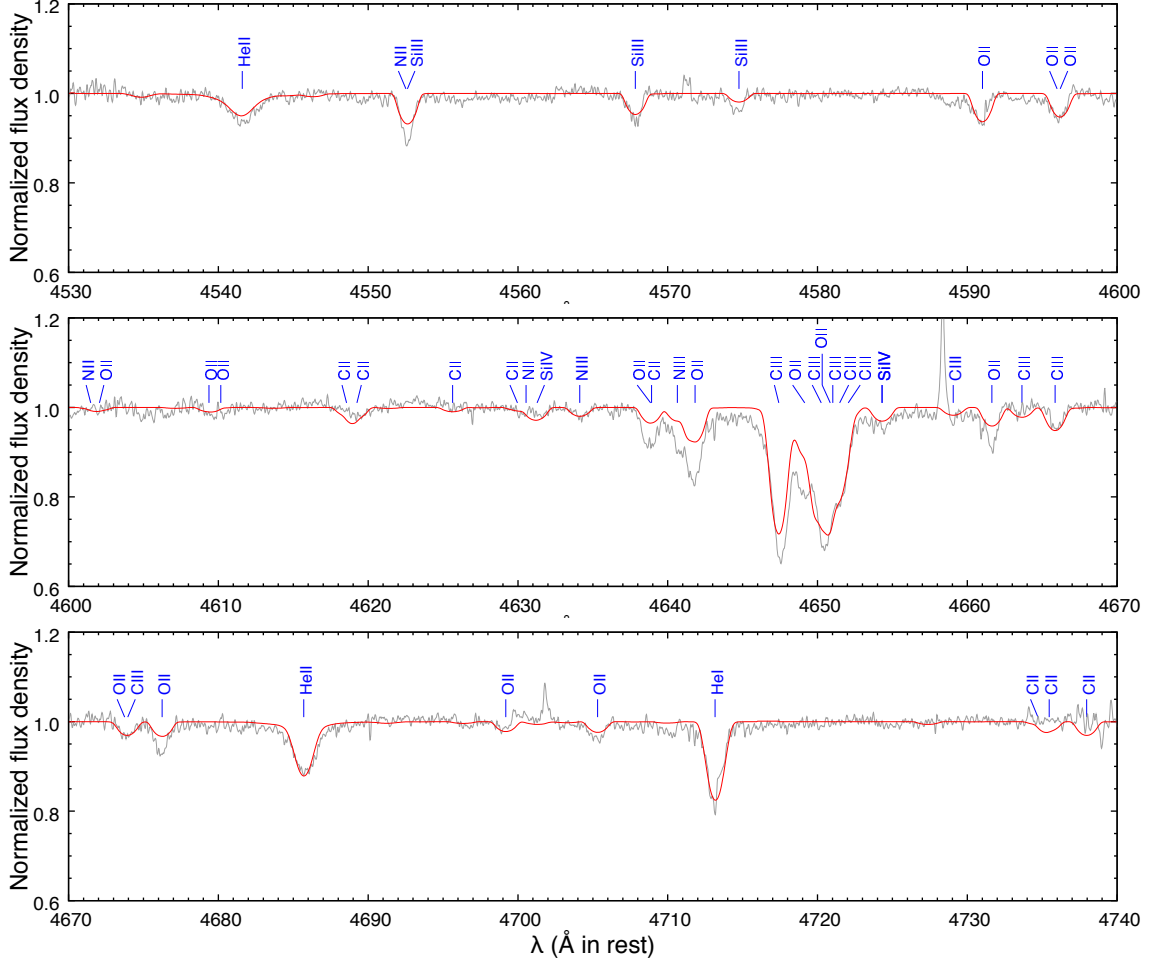


Figure 3. Comparison between the observed HDS (grey line) and the TLUSTY synthetic spectrum (red line) in the range between 4530 and 4740 Å. The absorption lines (except for H I) with the model predicted $EW \geq 10$ mÅ are indicated by the blue lines. The input parameters are listed in Table 5.

are not derived in optical HDS spectra of SaSt 2-3. These abundances are not small and also they are very important in characterising the spectrum of the central star and its radiation hardness (in particular, X-ray to UV wavelength). We know that the central star radiation is suppressed by the metal line-blanket effect and also it is very important in subsequent CLOUDY modelling. Thus, it is worth simulating these elements, too. We adopt the nebular Ne, S, Cl, and Ar abundances due to no detection of stellar absorption of these elements. We adopt $\epsilon(\text{Fe}) = 6.38$ ($[\text{Fe}/\text{H}] = -1.1$, see § 3.5). Based on the discussion in § 5, for the other elements up to Fe except for α -elements Mg, Ca, and Ti, we adopt the predicted values by the AGB nucleosynthesis model of initially $1.25 M_{\odot}$ and $Z = 0.001$ stars by Fishlock et al. (2014). For Mg, Ca, and Ti, we adopt $\epsilon(\text{Mg}) = 6.80$, $\epsilon(\text{Ca}) = 5.43$, and $\epsilon(\text{Ti}) = 4.05$, respectively (i.e., $[\text{Mg}, \text{Ca}, \text{Ti}/\text{H}] = -0.7$).

The stellar $\epsilon(\text{He}/\text{N}/\text{O})$ is in agreement with the nebular $\epsilon(\text{He}/\text{N}/\text{O})$ within their uncertainties. The stellar C/O ratio (2.93 ± 1.33) indicates that SaSt 2-3 is definitely a C-rich PN. Based on the consistency between the stellar and the nebular elemental abundances, we obtain an expected CEL $\epsilon(\text{C}) = 8.58 \pm 0.20$ using the CEL $\epsilon(\text{O})$ and the stellar C/O ratio.

4.2 Time variation of line-profile and radial velocity; Evidence of a binary central star

Our important discovery is that the central wavelength of the stellar absorption lines varies from date to date whereas there is no wavelength shift of the nebular emission lines.

We compute the heliocentric radial velocities v_r of the central star via Fourier cross correlation between the observed spectra and the synthetic TLUSTY spectrum using FXCOR in IRAF. FXCOR calculates the velocity shift between two different spectra in the selected wavelength regions¹³. Here, we select good S/N regions. In Table 6, we list v_r and $v_r - v_{\text{sys}}$, where v_{sys} is the systemic radial velocity measured from the 128 nebular emission lines ($+166.6 \text{ km s}^{-1}$, see § 3.1). In Fig. 4, we show the singlet He I 5015/7281 Å absorption and the TLUSTY synthetic spectrum as the guide.

We interpret that the radial velocity time-variation is caused by orbital motion in a binary system. Méndez et al. (1986) reported

¹³ The wavelength ranges we set are as follows; for the 2013 Oct 6 spectrum, 3911 – 3932, 4002 – 4036, 4082 – 4096, 4112 – 4182, 4302 – 4330, 4357 – 4442, and 4533 – 4730 Å. For the 2013 Dec 10, 5014 – 5023, 4920 – 4934, 5043 – 5056, 5403 – 5420, and 5589 – 5599 Å. For the 2016 Feb 1, 7280 – 7293 Å.

Table 6. Heliocentric radial velocity v_r of the central star. The systemic radial velocity v_{sys} is $+166.6 \text{ km s}^{-1}$ (§ 3.1).

Obs Date	JD (-2456000.0)	v_r (km s^{-1})	$v_r - v_{\text{sys}}$ (km s^{-1})
2013/10/06	573.096	$+152.8 \pm 0.6$	-13.76
2013/12/10	637.917	$+183.6 \pm 0.4$	$+16.95$
2016/02/01	1420.831	$+156.2 \pm 0.6$	-10.39

Table 7. Comparison between the derived abundances and the predicted values by the AGB nucleosynthesis models of Fishlock et al. (2014) for $1.25 M_{\odot}$ stars with $Z = 0.001$ and Karakas (2010) for $1.5 M_{\odot}$ stars with $Z = 0.004$. The CEL $\epsilon(\text{C})$ is the predicted value by our analysis (§ 4.1).

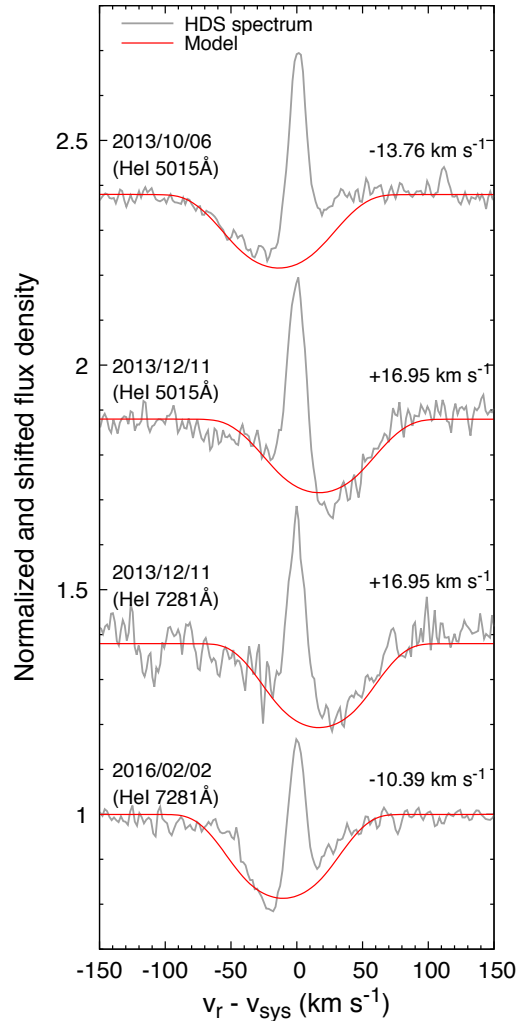
X	Nebular	Stellar	$1.25 M_{\odot}$ $Z = 0.001$	$1.50 M_{\odot}$ $Z = 0.004$
He	10.75 – 11.10	10.99 ± 0.09	11.01	10.97
C(RL)	9.21 ± 0.12	8.55 ± 0.10	8.56	8.46
C(CEL)	8.58 ± 0.20	...		
N	7.47 ± 0.06	7.25 ± 0.16	7.26	7.65
O	8.11 ± 0.04	8.10 ± 0.17	7.68	8.23
Ne	7.46 ± 0.04	...	7.37	7.42
Si	...	6.81 ± 0.10	6.39	6.85
S	6.10 ± 0.03	...	6.00	6.70
Cl	4.57 ± 0.07	...	4.08	...
Ar	5.66 ± 0.13	...	5.28	...
Fe	5.29 ± 0.06	...	6.38	6.80

the photometric and radial velocity variations of the CSPN of C₆₀ PN IC 418. They measured the radial velocities using the stellar C III 5695 Å and C IV 5801/11 Å. The systemic radial velocity was derived using the nebular [N II] 5755 Å line. Later, Méndez (1989) concluded that the central star is not likely to be a binary because the orbital motion alone (if present) would not be enough to explain the observed variations. We note that the C III 5695 Å and C IV 5801/11 Å lines are good indicators of the stellar activity (e.g., wind velocity) and these lines would be unlikely to give more accurate radial velocity of the central star. Thus, as far as we know, this would be the firm detection case of the binary central stars amongst all the C₆₀ PNe. Since we have only three periods of the binary motion, we do not determine any parameters of the binary central star yet.

We expected near-IR excess from the binary circumstellar disc from Otsuka et al. (2016) who detected near-IR excess in most of the SMC C₆₀ PNe and discussed possible links between near-IR excess, disc, and fullerene formation; since the ejected material from the central star can be stably harboured for a long time, even smaller molecules could aggregate into much larger molecules. However, in SaSt 2-3, we do not find near-IR excess in the observed SED (Fig. 1). No near-IR excess might mean a possibility of a nearly edge-on disc rather an inclined disc.

5 COMPARISON WITH AGB MODEL PREDICTIONS

In Table 7, we compile the derived abundances. The nebular CEL $\epsilon(\text{C})$ is an expected value by our analysis (§ 4.1). As the comparisons, we list the AGB nucleosynthesis model predictions by Fishlock et al. (2014) for initially $1.25 M_{\odot}$ stars with $Z = 0.001$ and Karakas (2010) for initially $1.50 M_{\odot}$ stars with $Z = 0.004$. Note that Fishlock et al. (2014) and Karakas (2010) set the initial $[\text{X}/\text{H}]$ to be -1.1 and -0.7 , respectively. We calculate reduced chi-squared values (χ^2_{ν} , ν is degree of freedom) between the nebular $\epsilon(\text{X})$ and the AGB model predicted values for each of $1.00 - 3.25 M_{\odot}$ star with $Z = 0.001$ (9 models in total).

**Figure 4.** Time-variation of the singlet He I line-profiles taken in three nights. The systemic radial velocity (v_{sys}) is $+166.6 \text{ km s}^{-1}$ (§ 3.1). The synthetic spectrum is overlotted. The heliocentric radial velocity v_r with respect to v_{sys} is indicated (see Table 6).

We use χ^2_{ν} as the guide to find out which AGB model's predicted abundances is the closest to the derived abundances. The aim of this analysis is to infer the initial mass of the progenitor. We should note that these AGB grid models do not aim to explain the observed elemental abundances of SaSt 2-3. We exclude Fe in χ^2_{ν} evaluation. We adopt the nebular $\epsilon(\text{X})$ values. For $\epsilon(\text{He})$ and $\epsilon(\text{C})$, we adopt 10.96 ± 0.17 (intermediate value, $9.10(-2) \pm 3.52(-3)$) and 8.58 ± 0.20 (an expected nebular CEL C value, $3.80(-4) \pm 1.76(-4)$), respectively.

Since the reduced- χ^2 for the $1.25 M_{\odot}$ model marks the minimum ($\chi^2_{\nu} = 14$ ($= 99/(8 - 1)$) in 8 elements), this model is the closest to the derived $\epsilon(\text{X})$. χ^2_{ν} is 17 ($= 66/(5 - 1)$) limited to $\epsilon(\text{He}/\text{C}/\text{N}/\text{O}/\text{Ne})$. Next, we compare the AGB models for the same mass stars with $Z = 0.004$ because these models could account for the derived abundances except for S (no predictions for Cl and Ar, however). The model for $1.5 M_{\odot}$ initial mass stars with $Z = 0.004$ gives the closest fit to the observation ($\chi^2_{\nu} = 360$ ($= 1800/(6 - 1)$) in 6 elements). Limited to $\epsilon(\text{He}/\text{C}/\text{N}/\text{O}/\text{Ne})$, χ^2_{ν} is 7 ($= 28/(5 - 1)$).

The B-type central star indicates that SaSt 2-3 is an extremely young PN and just finished the AGB phase. The presence of H absorption lines (Fig. 3) indicates that SaSt 2-3 did not experience

very late thermal pulse evolution, so this PN is probably in the course of H-burning post-AGB evolution. According to the H-burning post-AGB evolution model of Vassiliadis & Wood (1994), stars with initially $1.5 M_{\odot}$ and $Z = 0.004$ would evolve into hot stars with the core mass (M_*) of $0.64 M_{\odot}$. L_* of such stars is $\sim 7380 L_{\odot}$ when T_{eff} is $\sim 28\,100$ K in ~ 1050 years after the AGB phase. Whereas, we infer that $1.25 M_{\odot}$ stars with $Z = 0.001$ would evolve into stars with M_* of $0.649 M_{\odot}$; their L_* and T_{eff} is $\sim 7765 L_{\odot}$ and $\sim 28\,100$ K, respectively in ~ 1770 yrs after the AGB-phase based on the models of Fishlock et al. (2014) and Vassiliadis & Wood (1994). The main difference in the post-AGB evolution of $1.50 M_{\odot}/Z = 0.004$ stars and $1.25 M_{\odot}/Z = 0.001$ stars is evolutionary timescale.

Through these discussions, we summarise as follows. The $Z = 0.001$ model gives the closest values to the derived elemental abundances, although there is systematically ~ 0.3 – 0.4 dex discrepancy of $\epsilon(\text{O,Cl,Ar})$. The $Z = 0.004$ model shows excellent fit to the derived nebular and stellar $\epsilon(\text{He/C/N/O/Si})$. Considering initial settings of $[X/H]$ in the models, we conclude that the progenitor of SaSt 2-3 would be a $\sim 1.25 M_{\odot}$ star with initially $Z \sim 0.001$ ($[\text{Fe}/\text{H}] \sim -1.1$) and $[\alpha, \text{Cl}/\text{Fe}] \sim +0.3$ – 0.4 . This is consistent or comparable with the Galaxy chemical evolution model of Kobayashi et al. (2011); in the Galactic thick disc, the predicted $[\text{Si}/\text{Fe}]$, $[\text{S}/\text{Fe}]$, $[\text{Cl}/\text{Fe}]$, and $[\text{Ar}/\text{Fe}]$ are $\sim +0.6$, $\sim +0.4$, ~ -0.3 , and $\sim +0.3$ in $[\text{Fe}/\text{H}] < -1$, respectively.

6 PHOTOIONISATION MODEL

In the previous sections, we characterised the central star and dusty nebula. In this section, we build the photoionisation model using CLOUDY and TLUSTY to be consistent with all the derived quantities, AGB nucleosynthesis model, and post-AGB evolution model. Below, we explain how to set each parameter in the model, and then we show the result.

6.1 Modelling approach

6.1.1 Distance

Since the distance D is an important parameter, we estimate it by our own method as explained below. We first extract the stellar spectrum from the observed HDS spectrum because the observed spectrum is the sum of the nebular emission lines and continuum and the central star's continuum. For this purpose, we scale the HDS spectrum flux density to match the APASS $Bg'Vr'i'$ bands. Then, we subtract the theoretically calculated nebular continuum from the scaled HDS spectrum. We utilise the NEBCONT code in the DISPO package of STARLINK v.2015A¹⁴ to generate the nebular continuum under adopting $I(\text{H}\beta) = 1.57(-12) \text{ erg s}^{-1} \text{ cm}^{-2}$ (§ 3.2), $T_e = 10^4$ K, $n_e = 2000 \text{ cm}^{-3}$ (Table 2), and $n(\text{He}^+)/n(\text{H}^+) = 1.09(-2)$ (Table A3). In Fig. 5(a), we show the scaled HDS spectrum and the synthetic nebular continuum. Fig. 5(b) displays the TLUSTY synthetic spectrum of the central star (in the case of $T_{\text{eff}} = 28\,100$ K) scaled to match the residual spectrum generated by subtracting the nebular continuum from the HDS spectrum.

Next, by integrating the scaled central star's synthetic spectra in $T_{\text{eff}} = 27\,800$ – $28\,400$ K (Table 5) by our TLUSTY analysis (§ 4.1) in over the wavelength, we obtain L_* as a function of D and T_{eff} for this T_{eff} range;

¹⁴ <http://starlink.eao.hawaii.edu/starlink>

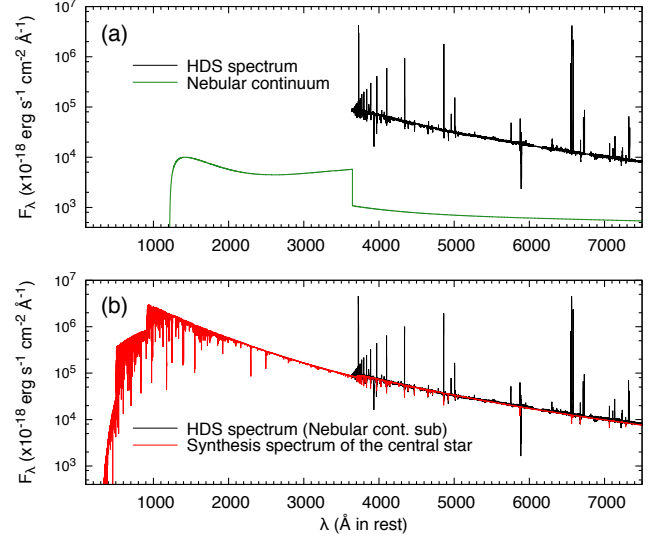


Figure 5. (Upper panel) The de-reddened HDS spectrum scaled up to the flux density at the APASS $Bg'Vr'i'$ bands and the calculated nebular continuum by NEBCONT. (Lower panel) The synthetic spectrum of the central star by TLUSTY (§ 4.1) scaled to match the residual spectrum produced by subtracting the nebular continuum from the HDS spectrum.

$$L_* = (48.56 \cdot (T_{\text{eff}}/10^4) - 75.94) \cdot D_{\text{kpc}}^2 L_{\odot}. \quad (2)$$

Assuming that the progenitor is an initially $1.25 M_{\odot}/Z = 0.001$ star and its luminosity is currently $7765 L_{\odot}$ (§ 5), we obtain $D = 9.90$ – 12.76 kpc. If we assume an initially $1.5 M_{\odot}$ progenitor star with $Z = 0.004$, D is 9.66 – 12.44 kpc.

In our CLOUDY model, we adopt $D = 11.33$ kpc, which is the intermediate value of D when we assume that the central star evolved from a star with initially $1.25 M_{\odot}$ and $Z = 0.001$. Adopting our measured Galactocentric distance of 17.35 kpc, the predicted $\epsilon(\text{O/Ne/Cl/S/Ar})$ from the Galaxy $\epsilon(\text{O/Ne/Cl/S/Ar})$ gradient established amongst Galactic PN nebular abundances by Henry et al. (2004) are 8.33 ± 0.21 , 7.61 ± 0.35 , 6.22 ± 0.25 , 4.67 ± 0.34 , and 6.06 ± 0.25 , respectively. These values are in line with the derived nebular abundances (Table 7). Our adopted $D = 11.33$ kpc is in agreement with Frew et al. (2016), who reported 14.86 ± 4.26 kpc. Our derived D is also comparable with the value (14.31 ± 8.54 kpc) determined from the parallax measured using *Gaia* DR2 ($\sigma_{\pi} = 0.0699 \pm 0.0417$ mas; *Gaia* Collaboration et al. 2018). Thus, we simultaneously justify our estimated D and nebular $\epsilon(\text{O/Ne/Cl/S/Ar})$.

6.1.2 Central star

As input to CLOUDY, we use the TLUSTY synthetic spectrum of the central star, adopting the parameters from Table 5. In our iterations here, we only vary T_{eff} in the range of $27\,800$ – $28\,500$ K and L_* in the range of 7300 – $8300 L_{\odot}$.

6.1.3 Nebula geometry and boundary condition

We plot the observed data and its interpolated curve in Fig. 6. The continuum spectrum in the wavelength $\lesssim 0.36 \mu\text{m}$ corresponds to the sum of (1) the nebular continuum (green line in Fig. 5(a)) and

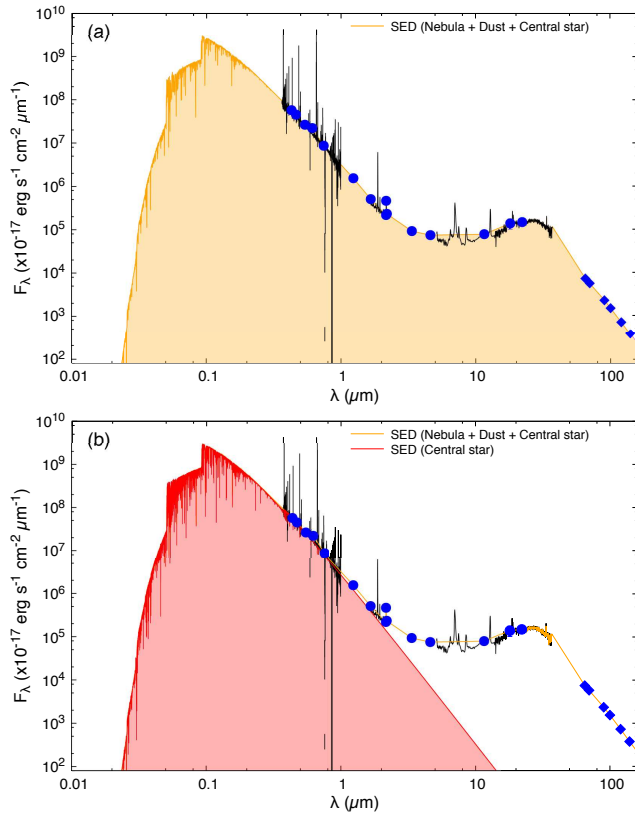


Figure 6. (Upper panel) SED based on the observed data (black lines and blue filled circles) and its interpolated curve (orange line). The far-IR flux density at 65, 90, 100, 120, and 140 μm (the blue diamonds) is an expected value. The integrated flux density between $\sim 5(-3)$ to 140 μm (indicated by the orange region) is $\sim 8215 L_{\odot}$ in $D = 11.33$ kpc. (Lower panel) SED based on the observed data and its interpolated curve, and the synthetic spectrum of the central star. The integrated flux density of the central star within the same wavelength range (indicated by the red region) is $\sim 7765 L_{\odot}$ in $D = 11.33$ kpc. See text in details.

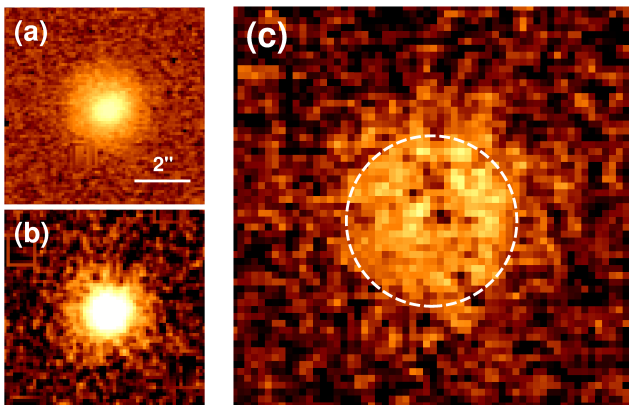


Figure 7. (LEFT two panels) The $\text{Br}\gamma$ and $\text{Br}\gamma_{45}$ images of SaSt2-3. (RIGHT panel) The $\text{Br}\gamma$ minus $\text{Br}\gamma_{45}$ image. The radius of the dashed circle is $1.2''$. North is up and east is left in these images.

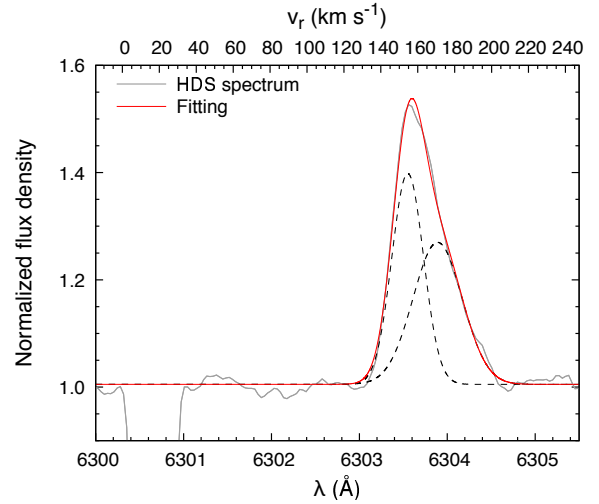


Figure 8. Fitting for the [O I] 6300 \AA line. This line can be fitted with two Gaussian components (dashed lines). The red line is the sum of these components.

(2) the synthetic spectrum of the central star (red line in Fig. 5(b)). The far-IR flux density at 65, 90, 100, 120, and 140 μm is an expected value obtained by fitting for the 15 – 40 μm *Spitzer*/IRS spectrum.

We use Equations (2) and (3) Otsuka et al. (2014), who fitted the *Spitzer*/IRS spectra of Galactic C_{60} PNe in 15 – 40 μm with the synthetic absorption coefficient Q_{λ} value. For SaSt 2-3, we set the minimum dust temperature = 20 K and adopt $p = q = 2$ and $\alpha = 0$ which are the same values used in Otsuka et al. (2014). From the fitting, we derive the maximum dust temperature of 136.2 ± 0.4 K, the expected F_{ν} at 65, 90, 100, 120, and 140 μm are 105.3, 63.5, 51.6, 35.0, and 24.6 mJy, respectively.

From integrating this SED (i.e., the orange region in Fig. 6(a)), we find a total luminosity of $\sim 8215 L_{\odot}$. The luminosity of each component is

Central star: $\sim 7765 L_{\odot}$,

Nebular continuum + dust continuum: $\sim 392 L_{\odot}$,

Nebular emission line: $\sim 58 L_{\odot}$.

Here, the luminosity of nebular emission line is the sum of all the detected emission lines in the HDS and *Spitzer* spectra. We obtain L_{*} of $\sim 7765 L_{\odot}$ by integrating flux density of the central star's SED within the same wavelength range, indicated by the red region in Fig. 6(b). Thus, we find that only ~ 6 percent of the central star's radiation ($= (392+58)/7765$) seems to be absorbed by the nebula.

To check whether nebula boundary is determined by the power of the stellar radiation (i.e., ionisation bound) or material distribution (i.e., material bound), we tested both the ionisation boundary model and the material boundary model. The WHIRC $\text{Br}\gamma$ and $\text{Br}\gamma_{45}$ images in Fig. 7 display the central bright region and the compact nebula. From the $\text{Br}\gamma - \text{Br}\gamma_{45}$ image (Fig. 7(c)), we measure the radius of the ionised nebula extended up to be $1.2''$.

The material boundary model (the model calculation is stopped at the outer radius of $1.2''$) gives a good fit except for underestimates of the [O I] and [N I] line fluxes. However, when we adopt an open geometry such as a cylinder in the ionisation boundary model (the model calculation is stopped when T_e is dropped down to ~ 4000 K where most of the ionised species are not emitted), we explained well the balance between the input energy from the central star and the output energy from the nebula plus dust

(i.e., $L_* \gg L_{\text{neb+dust}}$) and the observed [O I] and [N I] line fluxes. Although the WHIRC images do not clearly show a cylinder or bipolar nebula, it is plausible judging from the [O I] 6300 Å line-profile. Fig. 8 shows the [O I] 6300 Å line-profile fitting by two Gaussian components with $v_r = +154.6$ and $+170.6$ km s⁻¹ at the peak intensity of each component. The [O I] lines emitted from the most outer part of the nebula show blue-shifted asymmetry. Such asymmetric profiles are seen in e.g., PN Wray 16-423 (Otsuka 2015); Wray16-423 has a bright cylindrical structure surrounded by an elliptically extended nebula shell.

From these discussions, we adopt the cylinder geometry with the height = 0.8". We determined this scale height through a small grid model, and we found that the cylinder height $\geq 0.8''$ is necessary. We adopt ionisation bounded condition, assuming the ionisation front radius of 1.2".

6.1.4 Elemental abundances and hydrogen density

We adopt the nebular value of $\epsilon(\text{N/O/Ne/S/Cl/Ar/Fe})$ (Table 7) as the initial value and then refine via model iterations within 0.2 dex of the input values so that the best-fit abundances would reproduce the observed emission line intensities. We adopt the nebular $\epsilon(\text{He}) = 10.96$ as the first guess, and vary it in range from 10.75 to 11.10. We keep an expected CEL $\epsilon(\text{C}) = 8.58$ (c.f. stellar $\epsilon(\text{C}) = 8.55$) and stellar $\epsilon(\text{Si}) = 6.81$ through the model iterations. For α -elements Mg, Ca, and Ti (not derived, though), we fix the $[\text{Mg,Ca,Ti/Fe}] = +0.3$, where $[\text{Fe/H}]$ is -1.1 (§ 5). We adopt a constant hydrogen number density (n_{H}) radial profile. We first guess that n_{H} is equal to n_e ; we adopt the average n_e amongst the measured n_e except for $n_e([\text{N I}])$ (Table 2), then we vary n_{H} to get the best fit.

6.1.5 Dust grains

We assume that the underlying continuum is due to graphite grains based on the fact that SaSt 2-3 shows the spectral signature of carbon-rich species.

We use the optical data of Martin & Rouleau (1991) for randomly oriented graphite spheres, and we assume the "1/3 - 2/3" approximation (Draine & Malhotra 1993). We adopt the grain radius $a = 0.05 - 0.25 \mu\text{m}$ and $a^{-3.5}$ size distribution. If we set the smallest $a = 0.005 \mu\text{m}$, the maximum grain temperature is over the sublimation temperature of 1750 K. Thus, we set the smallest $a = 0.05 \mu\text{m}$. We resolve the size distribution into 20 bins (the smallest is $0.05 - 0.054 \mu\text{m}$ and the largest is $\sim 0.23 - 0.25 \mu\text{m}$). We do not attempt to fit the broad $6 - 9 \mu\text{m}$ and $11 \mu\text{m}$ features because the carriers of these features are not determined yet and also these profiles are different from typical band profile of the polycyclic aromatic hydrocarbons (PAHs) in the same wavelengths.

6.2 Modelling results

The input parameters of the best fitting result and the derived quantities are summarised in Table 8. In total, we varied 12 parameters within a given range; L_* , $\epsilon(\text{He/N/O/Ne/S/Cl/Ar/Fe})$, inner radius (r_{in}), n_{H} , and grain abundance until χ^2_{ν} calculated from $I(\text{H}\beta)$, 76 emission line fluxes, 25 broadband fluxes, 4 mid-IR flux densities, and ionisation bound radius (i.e., outer radius r_{out}). Since there is no observed far-IR data, we stop the model calculation at the ionisation front, where T_e is dropped down to ~ 4000 K. To evaluate the goodness of the model fitting, we refer to χ^2_{ν} . For the [O I] and [N I] lines, we adopt 30 percent relative uncertainty because these

Table 8. The best-fit model parameters of SaSt 2-3.

Central star	Value
$L_* / T_{\text{eff}} / \log g / D$	$7400 L_{\odot} / 28\,170 \text{ K} / 3.11 \text{ cm s}^{-2} / 11.33 \text{ kpc}$
$M_V / R_* / m_*$	$-2.10 / 3.606 R_{\odot} / 0.611 M_{\odot}$
Nebula	Value
Geometry	Cylinder with height = 0.8" (8600 AU)
Radius	$r_{\text{in}}: 0.006''$ (63 AU), $r_{\text{out}}: 1.25''$ (14 162 AU)
$\epsilon(\text{X})$	He: 10.83, C: 8.58, N: 7.46, O: 8.27, Ne: 7.46, Mg: 6.80, Si: 6.84, S: 6.10, Cl: 4.51, Ar: 5.65, Ca: 5.43, Ti: 4.05, Fe: 5.41, Others: Fishlock et al. (2014)
n_{H}	3098 cm^{-3}
$\log I(\text{H}\beta)$	$-11.804 \text{ erg s}^{-1} \text{ cm}^{-2}$
m_g	$6.13(-2) M_{\odot}$
Dust	Value
Grain size	$0.05 - 0.25 \mu\text{m}$
$T_d / m_d / \text{DGR} (m_d/m_g)$	$66 - 909 \text{ K} / 2.08(-5) M_{\odot} / 3.39(-4)$

Note – Nebular $\epsilon(\text{He/N/O/Ne/S/Cl/Ar/Fe})$ abundances derived by empirical method (§ 3.5) are 10.75 – 11.10/7.47/8.11/7.46/6.10/4.57/5.66/5.29, respectively.

Table 9. Ionic abundance fraction predicted by our model and comparison between the predicted ICFs ($\text{ICF}_{\text{model}}$) and the empirically determined ICFs (ICF_{emp}).

X	X ⁰	X ⁺	X ²⁺	X ³⁺	$\text{ICF}_{\text{model}}$	ICF_{emp}
He	0.845	0.155	< 0.001		6.70	5.12 – 11.57
C	< 0.001	0.883	0.116	< 0.001	8.61	5.12 ± 1.41
N	0.002	0.948	0.050	< 0.001	1.05	1.04 ± 0.13
O	0.010	0.982	0.008	< 0.001	1.01	1.00
Ne	0.012	0.988	< 0.001	< 0.001	1.01	1.00
S	< 0.001	0.244	0.756	< 0.001	1.00	1.00
Cl	< 0.001	0.383	0.617	< 0.001	1.00	1.00
Ar	0.003	0.867	0.131	< 0.001	7.66	5.12 ± 1.41
Fe	< 0.001	0.062	0.923	0.015	1.08	1.31 ± 0.16

lines are mostly from the PDRs. For the higher order Balmer lines H1 (B24 - B14), we set 10 percent relative uncertainty by considering into account the uncertainty of these lines largely affected by the stellar absorption. The reduced- χ^2 value in the best model is 12. The relatively large reduced- χ^2 value even in the best fitting would be due to the uncertainty of the atomic data which we cannot control. Therefore, we conclude that our best fitting result reproduces observations very well. The predicted line fluxes, broadband fluxes, and flux densities are compiled in Appendix Table A5. For references, we list *expected* F_{ν} at 65, 90, 100, 120, and 140 μm obtained by fitting for the 15 – 40 μm *Spitzer/IRS* spectrum (§ 6.1.3). In Figs. 9 and 10, we compare the model SED with the observed one.

In Fig. 11, we show the location of the CSPN predicted by our CLOUDY model on the post-AGB evolutionary tracks for initially $Z = 0.001$ and 1.0, 1.25, and 1.50 M_{\odot} (Vassiliadis & Wood 1994). We generate this 1.25 M_{\odot} track by linear interpolation between the 1.00 and 1.50 M_{\odot} tracks of (Vassiliadis & Wood 1994). Our CLOUDY model predicts $L_* = 7400 L_{\odot}$, $T_{\text{eff}} = 28\,170 \text{ K}$, and $m_* = 0.611 M_{\odot}$. L_* and m_* are justly close to predicted values ($\sim 7765 L_{\odot}$ and 0.649 M_{\odot}) based on the models of initially 1.25 M_{\odot} stars with $Z = 0.001$ (Vassiliadis & Wood 1994; Fishlock et al. 2014). In Fig. 11, we plot the model results of Gesicki & Zijlstra (2007) and Otsuka et al. (2014) as well. These two models show a large discrepancy from the predicted post-AGB evolution track, but our model completely improves this.

Our model succeeds in reproducing the derived $\epsilon(\text{X})$, the vol-

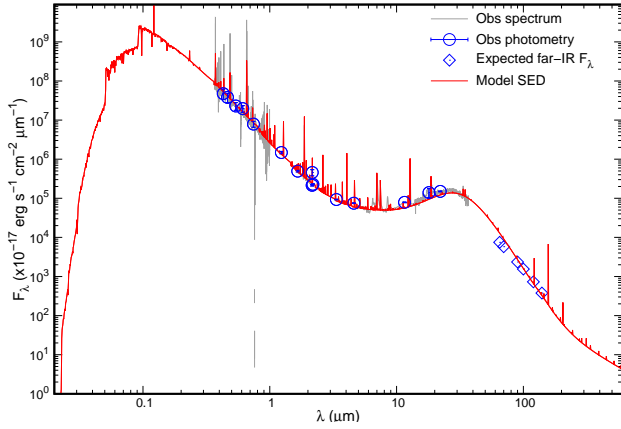


Figure 9. Comparison between the observed SED (blue circles and grey lines) and the SED predicted by the best fit model (red line). The spectral resolution (R) of the model SED is a constant 1000.

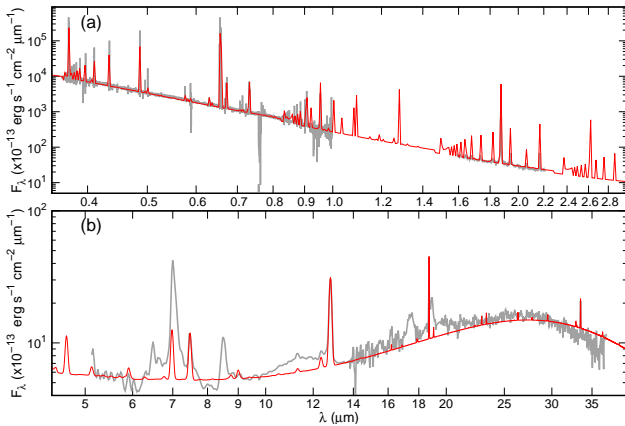


Figure 10. Comparison between the observed SED and the SED predicted by the best fit model in $0.35 - 3.0\mu\text{m}$ (upper panel) and in $4.4 - 40\mu\text{m}$ (lower panel). The legends in both panels are the same used in Fig. 9. R of the model SED in $0.35 - 3.0\mu\text{m}$ is a constant 1000. R is a constant 90 in $4.4 - 14\mu\text{m}$ (low-resolution module) and 570 in $14 - 40\mu\text{m}$ (high-resolution one), which correspond to the *Spitzer*/IRS resolution.

ume average T_e (9150 K, while 8930 K in the observation), and $I(\text{H}\beta)$. In Table 9, we present the fraction of each ion in each element. Except for C and Ar, the model predicted ICF is well consistent with the empirically determined ICF.

The gas mass m_g is the sum of the ionised and neutral atomic/molecular gas species. Note that we stopped the model calculation at the ionisation front. Our m_g is ~ 18 percent of the ejected mass at the last thermal pulse (TP) of $1.25 M_\odot$ initial mass stars with $Z = 0.001$ ($0.334 M_\odot$, Fishlock et al. 2014). If we increase the emitting volume by adopting a closed-geometry such as a spherical nebula, the situation is slightly improved (we trace ~ 35 percent of the ejected mass) but the fitting model becomes worse as we explained. According to Fishlock et al. (2014), such stars experienced the superwind phase in the final few TPs during which the mass-loss rate reaches a plateau of $\sim 10^{-5} M_\odot \text{yr}^{-1}$. One might think that our underestimated m_g might be caused by excluding the neutral gas and molecular gas regions. However, it is unlikely that SaSt 2-3 has the molecular gas rich envelope because the molecular hydrogen H_2 lines in K -band are not detected (Lumsden et al. 2001).

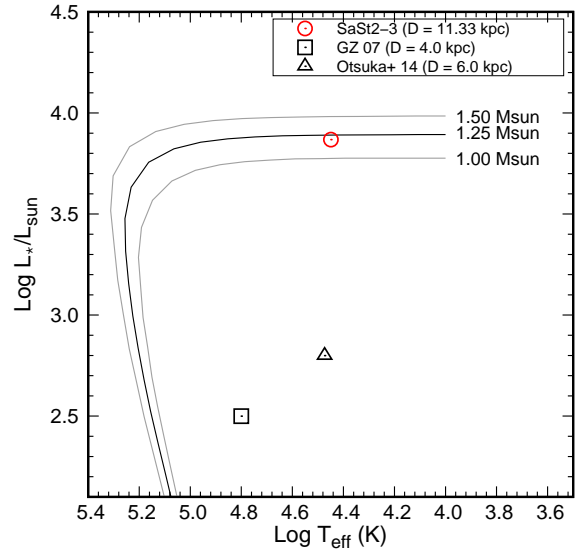


Figure 11. The location of the central star on the post-AGB evolutionary tracks for initially $Z = 0.001$ and 1.0 , 1.25 , and $1.50 M_\odot$ (Vassiliadis & Wood 1994). We generate this $1.25 M_\odot$ track by linear interpolation between the 1.00 and $1.50 M_\odot$ tracks of Vassiliadis & Wood (1994). For comparisons, we plot T_{eff} and L_* of the central star derived by Gesicki & Zijlstra (2007) (GZ07, square; $T_{\text{eff}} = 63\,095$ K and $L_* = 316 L_\odot$ under $D = 4$ kpc) and Otsuka et al. (2014) (Otsuka+ 14, triangle; $T_{\text{eff}} = 29\,750$ K and $L_* = 630 L_\odot$ under $D = 6$ kpc).

Indeed, we confirm this fact by analysis of the UKIRT CGS4 HK -band spectrum of SaSt 2-3 (Fig. 1). Since our m_g is greater than the ejected mass $2.7(-3) M_\odot$ at the last TP of initially $1.00 M_\odot$ stars with $Z = 0.001$, we can conclude that the progenitor should be a $> 1.00 M_\odot$ initial mass star. Fishlock et al. (2014) predicts that $1.00 M_\odot$ stars lost the majority of its stellar envelope before it reaches the superwind phase. The $1.25 M_\odot$ progenitor that we infer might have experienced such mass loss. If this is true, non-detection of the H_2 lines might be because thin circumstellar envelope does not shield UV radiation from the CSPN and H_2 is dissociated. As an other explanation for the estimated small m_g , the ejected mass during the AGB phase might be efficiently transported to the stellar surface of a companion star. Our small m_g would be largely improved by taking cold gas/dust components that can be traced by far-IR observation.

As presented in Fig. 10(b), our CLOUDY model predicts an emission line around $7\mu\text{m}$. This line is the complex of the $[\text{Ar II}] 6.99\mu\text{m}$ and $\text{H} 16.95/7.09\mu\text{m}$ lines. In the *Spitzer*/IRS spectrum, we measure the total line-flux of the $[\text{Ar II}] 6.99\mu\text{m}$, $\text{H} 16.95/7.09\mu\text{m}$, and $\text{C}_{60} 7.0\mu\text{m}$ to be 28.67 ± 3.23 , where $I(\text{H}\beta) = 100$. The model predicts $I([\text{Ar II}] 6.99\mu\text{m} + \text{H} 16.95/7.09\mu\text{m})/I(\text{H}\beta) = 4.173$ ($I(\text{H}\beta) = 100$). The contribution of the atomic line complex to the $\text{C}_{60} 7.0\mu\text{m}$ band (14.6%) is not as significant as Otsuka et al. (2014) expected (30.3%). We estimate $I(\text{C}_{60} 7.0\mu\text{m})/I(\text{H}\beta)$ to be 24.5 ± 2.8 .

7 DISCUSSIONS

7.1 Evolution of SaSt 2-3

Using the Galactic rotation velocity based on the distance scale of Cahn et al. (1992), van de Steene & Zijlstra (1995), and Zhang (1995), $v_r(\text{LSR}) = 149.1 \text{ km s}^{-1}$, and $D = 11.33 \text{ kpc}$, we obtain

Table 10. Nebular and central star’s properties of C₆₀-containing PNe IC 418, Tc 1 and SaSt 2-3 and non C₆₀-containing C-rich PNe, IC 2165 and Me 2-1. $\epsilon(\text{He})$ in SaSt 2-3 listed in this table is the intermediate value of $\epsilon(\text{He})$ derived by empirical method. M_{ini} is the initial mass of the progenitor inferred from the plot of L_* and T_{eff} on the post-AGB evolutionary tracks (Fig. 12) based on Vassiliadis & Wood (1994).

Nebula	$\epsilon(\text{He})$	$\epsilon(\text{C})$	$\epsilon(\text{N})$	$\epsilon(\text{O})$	$\epsilon(\text{Ne})$	$\epsilon(\text{S})$	$\epsilon(\text{Cl})$	$\epsilon(\text{Ar})$	$\epsilon(\text{Fe})$	Z	$\log L_*/L_\odot$	T_{eff} (K)	$\log g$ (cm s ⁻²)	M_{ini} (M _⊙)
IC 418	11.08	8.90	8.00	8.60	8.00	6.65	5.00	6.20	4.60	0.008	3.88	36 700	3.55	~1.8
Tc 1	10.92	8.56	7.56	8.41	7.80	6.45	4.97	6.08	5.19	0.004	3.85	32 000	3.30	~1.5
SaSt 2-3	10.96	8.58	7.47	8.11	7.46	6.10	4.57	5.66	5.29	0.001	3.87	28 170	3.11	~1.3
IC 2165	11.05	8.62	8.07	8.53	7.73	6.26	...	6.00	...	0.004	3.73	181 000	7.0	~2.1
Me 2-1	11.00	8.85	7.71	8.72	7.97	6.96	...	6.20	...	0.008	3.56	170 000	7.0	~1.8

Note – We estimated L_\odot of Tc 1 using $D = 3.0$ kpc (cf. 2.67 kpc, Frew et al. 2013), a theoretical model spectrum of Lanz & Hubeny (2007) for O-type stars with $T_{\text{eff}} = 32\,000$ K, $\log g = 3.3$ cm s⁻² (Mendez et al. 1992), and $Z = 0.008$ to match with the interstellar extinction corrected *HST*/STIS spectrum of the central star (Khan & Worthey 2018). We estimated T_{eff} of IC 2165 and Me 2-1 based the energy balance method of Dopita & Meatheringham (1991). L_* is estimated using theoretical model spectra of Rauch (2003) with the derived T_{eff} and assumed $\log g = 7.0$ cm s⁻² to match with the dereddened *HST*/WFPC2 F547M/F555W (*V*-band) magnitude of the central stars measured by Wolff et al. (2000), and D of Frew et al. (2013).

$\Delta V = 68.2 - 77.9$ km s⁻¹. The height above the Galactic plane $|z|$ is 1.13 kpc. These results are in agreement with the Type III PN classification of Quireza et al. (2007). ΔV and $|z|$ do not exceed 120 km s⁻¹ and 1.99 kpc for the Type IV PN classification of Quireza et al. (2007), respectively. The metallicity of SaSt 2-3 is much richer than typical halo PNe such as K 648, BoBn 1, and H 4-1 showing $[\text{Ar}/\text{H}] \lesssim -2$ (Otsuka et al. 2010, 2015; Otsuka & Tajitsu 2013). Thus, we conclude that SaSt 2-3 belongs to the thick disc younger population and a Type III PN rather than a Type IV PN (Pereira & Miranda 2007). Note that classification of PN type does not matter whether the central star is binary or not.

SaSt 2-3 would have evolved from a binary composed of a $\sim 1.25 M_\odot$ initial mass star and an companion star. However, any parameters on binary motion are unknown yet. According to the simulation using the `binary_c`¹⁵ code by Izzard et al. (2004), an initially $1.25 M_\odot$ single star with $Z = 0.001$ will enter the PN phase within 3.5 Gyr after the progenitor was in the main-sequence. Perhaps, evolutionary time required to reach the AGB phase would be shortened by binary interaction (i.e., < 3.47 Gyr).

SaSt 2-3 composes of a $\sim 0.61 M_\odot$ B-type cool central star with $T_{\text{eff}} = 28\,100$ K and a companion star. We find the Ca I absorption centred at 6616.62 Å and 6689.28 Å in heliocentric wavelength (6613.13 and 6685.6 Å in rest wavelength, respectively). v_r using these two absorption lines is 165.5 km s⁻¹ and 152.1 km s⁻¹, respectively. These v_r is close to v_r of the central star (183.6 km s⁻¹, Table 6). Thus, we assume that these lines could be originated from the envelope in the companion star. However, since there is only one spectrum covering 6600 – 6690 Å we have (Table 1), we do not yet find radial velocity variations of this absorption. We suppose that the companion star might be a F-K spectral type star in the main-sequence in terms of the initial mass by referring to De Marco et al. (2013).

7.2 Comparisons with non-C₆₀ and C₆₀-containing PNe

Our study can fully characterise the physical properties of SaSt 2-3. Thus, we are able to compare nebular elemental abundances and central star properties with those of other C₆₀ PNe, and we attempt to gain insights into the C₆₀ formation in PNe. For this purpose, we select C₆₀ PNe Tc 1 and IC 418 because they were previously modelled using CLOUDY, and they have been extensively studied. In Table 10, we compile their properties. Due to the lack of

¹⁵ This code can simulate single star evolution by adopting a large binary separation and a small companion star. Here, we adopted an initial binary separation of $1(+6) R_\odot$ and the initial companion star mass of $0.1 M_\odot$.

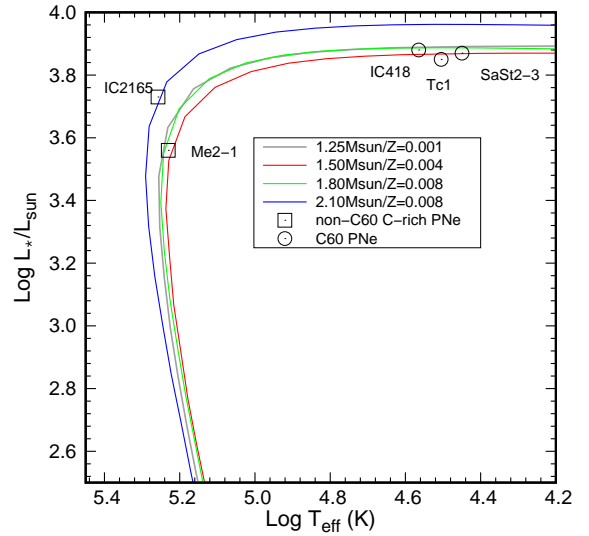


Figure 12. The location of C₆₀-containing PNe IC 418, Tc 1, and SaSt 2-3 and non-C₆₀ C-rich PNe IC 2165 and Me 2-1 on the post-AGB evolutionary tracks based on Vassiliadis & Wood (1994).

existing UV spectra, the CEL $\epsilon(\text{C})$ in SaSt 2-3 is not determined yet. However, since we adopt an expected CEL $\epsilon(\text{C}) (= (C/O)_* \times O_{\text{CEL}})$ from the stellar C/O ratio, the reliability of the discussion here is not compromised. We adopt the results of Tc 1 and IC 418 by Pottasch et al. (2011) and Morisset & Georgiev (2009), respectively. For Tc 1, since Pottasch et al. (2011) calculated $\epsilon(\text{Ar})$ by the sum of the Ar⁺ and Ar²⁺ abundances without subtracting C₆₀ 7.0 μm and H I lines from the complex line at 7 μm, their calculated $\epsilon(\text{Ar})$ is certainly overestimated. Therefore, we compute $\epsilon(\text{Ar})$ from Ar²⁺ (7.0(-7)) and $\text{ICF}(\text{Ar}) = \text{S}/\text{S}^{2+}$ (1.71). $\epsilon(\text{He})$ in Tc 1 is predicted by their CLOUDY model.

Comparisons with theoretical AGB nucleosynthesis models of Karakas (2010) indicate that the initial mass (M_{ini}) is $\sim 1.90 - 2.10 M_\odot$ for IC 418 and $\sim 1.50 - 1.90 M_\odot$ for Tc 1, respectively. From plots of L_* and T_{eff} on the post-AGB evolutionary tracks based on Vassiliadis & Wood (1994) (Fig. 12), we have the same estimate for IC 418 ($\sim 1.8 M_\odot$) and Tc 1 ($\sim 1.5 M_\odot$). Based on our estimates for the initial mass and metallicity, the age of IC 418 and Tc 1 after the main sequence is $\sim 2 - 3$ Gyr. Thus, we attest that SaSt 2-3 is the most metal-deficient and oldest Galactic C₆₀ PN.

Our findings in elemental abundances are as follows; (i) the values of $\epsilon(\text{C})$ in these C₆₀ PNe are not peculiar values that can be explained by the AGB nucleosynthesis models, (ii) despite that the C₆₀ band strength in SaSt 2-3 and Tc 1 is much stronger than

that in IC 418 (see Table 10 of [Otsuka et al. 2014](#)), and $\epsilon(\text{C})$ in Tc 1 and SaSt 2-3 is smaller than that in IC 418, and (iii) the C/O ratio (an indicator of the amount of the C-atoms unlocked in dust and molecules) in Tc 1 is smaller than that in IC 418. Supporting (i), non C_{60} -containing C-rich PNe IC 2165 ([Miller et al. 2018](#)) and Me 2-1 ([Pottasch & Bernard-Salas 2010](#)) (they are selected based on metallicity and initial mass) show similar abundances (including $\epsilon(\text{C})$) to C_{60} PNe. The difference between non- C_{60} and C_{60} PNe is T_{eff} only, supporting that the weak radiation field from the central star is in favour of the C_{60} formation. The time during which C_{60} is present might be a short-lived phase that C-rich PNe go through, but we do not yet have firm observational evidence of this. These findings would result in our conclusion that the C_{60} formation does not largely depend on the amount of the C-atoms produced during the AGB phase, and Tc 1 and SaSt 2-3 efficiently produced the C_{60} molecule by some mechanisms not present in IC 418.

It is noticeable that Fe abundance is highly depleted in all C_{60} PNe. The highly deficient Fe is possibly due to selective depletion in a binary disc (e.g., [Otsuka et al. 2016](#), reference therein). If C_{60} PNe have a disc around the central star, they can harbour mass-loss including AGB products for a long time and shield C_{60} molecules from the intense central star's UV radiation. Then, most of the Fe-atoms might be tied up in dust grains (e.g., FeO) within a disc. Accordingly, an environment suitable for large carbon molecule formation might be created. This would be in the case of SaSt 2-3. The central star of IC 418 would be not a binary (e.g., [Méndez 1989](#)). There are no reports on the binary central star of Tc 1 so far.

If it is the case, is C_{60} formation dependent on the central star's properties and its surrounding environment, such as a binary disc? To answer this question, we need to calculate the mass of the C-atoms present in atomic gas, dust and C_{60} by a fair means. From a more global perspective, the fraction of the C-atoms would be a critically important parameter to understand how much mass carbon PN progenitors had returned to their host galaxies. However, we find that the excitation diagram based on the observed C_{60} 8.5/17.4/18.9 μm fluxes and the expected C_{60} 7.0 μm flux ($I(\text{C}_{60} 7.0 \mu\text{m})/I(\text{H}\beta) = 24.5 \pm 2.8$, see § 6.2) in SaSt 2-3 indicates non-LTE conditions. The same situation exists in other C_{60} PNe including Tc 1 ([Cami et al. 2010](#)) and IC 418 ([Otsuka et al. 2014](#)). Therefore, we sought other ways not involving the excitation diagrams. Of these, the method proposed by [Berné & Tielens \(2012\)](#) is seemingly suitable to our aim; this method requires the observed/modelled IR SED, all four mid-IR C_{60} band fluxes, and dust mass. These three parameters are already determined in SaSt 2-3 and IC 418.

In Table 11, we summarise the mass of the C-atoms present in atomic gas, dust, and C_{60} in SaSt 2-3, IC 418, and Lin 49 in the SMC (as a comparison of the possible binary C_{60} PN). For SaSt 2-3 and Lin 49, we obtain $I(\text{IR})$ by integrating the atomic gas emission free SED (generated by the CLOUDY best model) in the range from 4 to 200 μm . Then, we calculate the total C_{60} flux $I(\text{C}_{60})$ (Table A1). Finally, assuming that the dust and C_{60} are emitted in the same regions, we estimate the C_{60} mass ($= m_d \times I(\text{C}_{60})/I(\text{IR})$). The column density and total number of C_{60} in SaSt 2-3 are 8.57(+12) cm^{-2} and 7.53(+47), respectively. By applying the method to IC 418 (but using the combined Infrared Space Observatory (ISO)/Short Wavelength Spectrometer (SWS)/Long-Wave Spectrometer (LWS) and *Spitzer* combined spectrum), we obtain their C_{60} mass.

From this analysis, we quantitatively demonstrate that SaSt 2-3 and Lin 49 produced C_{60} more efficiently than IC 418. Thus, we conclude that the C_{60} formation depends upon the central star's

Table 11. Mass of the C-atoms in each atomic gas, dust, and C_{60} .

Nebula	atomic C ($\times 10^{-4} M_{\odot}$)	graphite grains ($\times 10^{-5} M_{\odot}$)	C_{60} ($\times 10^{-7} M_{\odot}$)	Mass frac. of C_{60} (%)
IC 418	3.99	1.70	2.26	0.05
Lin 49	3.00	4.15 – 4.29	3.05 – 4.64	0.09 – 0.14
SaSt 2-3	2.17	2.08	4.53	0.19

Note – Mass of C_{60} is determined by (graphite grain mass for Lin 49 and SaSt 2-3) or (the total dust mass 7.76(–5) M_{\odot} including graphite grain for IC 418; [Gómez-Llanos et al. 2018](#)) $\times I(\text{C}_{60})/I(\text{IR})$. $I(\text{C}_{60})$ is the total flux of the mid-IR C_{60} bands measured by [Otsuka et al. \(2014\)](#), 1.03(–10) $\text{erg s}^{-1} \text{cm}^{-2}$ for IC 418 using the ISO/SWS/LWS and *Spitzer* combined spectrum), [Otsuka et al. \(2016\)](#), 9.26(–14) $\text{erg s}^{-1} \text{cm}^{-2}$ for Lin 49), and the present work for SaSt 2-3 (9.43(–13) $\text{erg s}^{-1} \text{cm}^{-2}$). $I(\text{IR})$ in IC 418, Lin 49, and SaSt 2-3 is 3.53(–8), 1.26(–11) (two-shell model)/8.56(–12) (single shell model), and 4.33(–11) in $\text{erg s}^{-1} \text{cm}^{-2}$, respectively.

properties and its surrounding environment (e.g., a binary disc), rather than the amount of C-atoms.

8 SUMMARY

We have studied the fullerene-containing PN SaSt 2-3 in order to investigate its physical properties and gain insights into the C_{60} formation in PN progenitors. We derived the nine and four elemental abundances from nebular line and stellar absorption analysis, respectively. The derived elemental abundances indicate that the progenitor is an initially $\sim 1.25 M_{\odot}$ star with $Z = 0.001$ and α -element and Cl enhanced ($[\alpha, \text{Cl}/\text{Fe}] \sim +0.3$ – 0.4). The distance D of 11.33 kpc is determined by comparing the derived luminosity as a function of D and T_{eff} with the predicted luminosity by the post-AGB evolution model for the $1.25 M_{\odot}$ stars with $Z = 0.001$. SaSt 2-3 is classified as part of the thick disc population with an early B-type central star with $T_{\text{eff}} = 28$ 100 K, $\log g = 3.11 \text{ cm s}^{-2}$, and the core-mass of $\sim 0.61 M_{\odot}$. We discovered the binary central star of SaSt 2-3 from time-variation of the stellar radial velocity. Further observations are necessary to understand the binary system. We built the comprehensive photoionisation model. The calculated gas mass is much smaller than the AGB model prediction for the single $1.25 M_{\odot}$ stars with $Z = 0.001$. The lower gas mass could be due to the short duration time of the superwind phase or efficient mass-transfer into the stellar surface of the companion star during the AGB phase. From the simple analysis, we quantitatively demonstrate that SaSt 2-3 produced C_{60} more efficiently than other C_{60} PNe. The C_{60} formation would depend on the central star's properties and its surrounding environment. There might be a link between the C_{60} formation efficiency and the binary central star. Spatially-resolved spectral maps of the atomic carbon, carbon dust, and C_{60} are necessary to identify the locations of C_{60} and investigate the abundance distribution of these species within dusty nebula. We succeed to demonstrate what type of and how much mass of stars can produce how much C_{60} molecules. We will further investigate stellar/nebular properties and C_{60} in order to find what parameters are of critical importance in the C_{60} formation.

ACKNOWLEDGEMENTS

I am grateful to the anonymous referee for carefully reading and the useful suggestions which greatly improved this article. I learned a lot of things from his/her comments. I was supported by the research fund 104-2811-M-001-138 and 104-2112-M-001-041-MY3

from the Ministry of Science and Technology (MOST), R.O.C. I thank Dr. Akito Tajitsu for supporting my Subaru HDS observations. I sincerely thank Drs. Benjamin Sargent, Peter Scicluna, and Toshiya Ueta for critically reading the paper and giving suggestions. This work was partly based on archival data obtained with the *Spitzer* Space Telescope, which is operated by the Jet Propulsion Laboratory, California Institute of Technology under a contract with NASA. This research is in part based on observations with *AKARI*, a JAXA project with the participation of ESA. A portion of this work was based on the use of the ASIAA clustering computing system.

REFERENCES

- Acker A., Marcout J., Ochsenbein F., Stenholm B., Tylenda R., Schohn C., 1992, The Strasbourg-ESO Catalogue of Galactic Planetary Nebulae. Parts I, II. European Southern Observatory, Garching, Germany
- Bernard-Salas J., Cami J., Peeters E., Jones A. P., Micelotta E. R., Groenewegen M. A. T., 2012, *ApJ*, **757**, 41
- Berné O., Tielens A. G. G. M., 2012, *Proceedings of the National Academy of Science*, **109**, 401
- Berné O., Montillaud J., Joblin C., 2015, *A&A*, **577**, A133
- Buton C., et al., 2013, *A&A*, **549**, A8
- Cahn J. H., Kaler J. B., Stanghellini L., 1992, *A&AS*, **94**, 399
- Cami J., Bernard-Salas J., Peeters E., Malek S. E., 2010, *Science*, **329**, 1180
- Cardelli J. A., Clayton G. C., Mathis J. S., 1989, *ApJ*, **345**, 245
- Cutri R. M. e., 2014, VizieR Online Data Catalog, **2328**
- Cutri R. M., et al., 2003, VizieR Online Data Catalog, **2246**
- De Marco O., Passy J.-C., Frew D. J., Moe M., Jacoby G. H., 2013, *MNRAS*, **428**, 2118
- Delgado-Inglada G., Rodríguez M., 2014, *ApJ*, **784**, 173
- Delgado-Inglada G., Morisset C., Stasińska G., 2014, *MNRAS*, **440**, 536
- Dopita M. A., Hua C. T., 1997, *ApJS*, **108**, 515
- Dopita M. A., Meatheringham S. J., 1991, *ApJ*, **377**, 480
- Draine B. T., Malhotra S., 1993, *ApJ*, **414**, 632
- Duley W. W., Hu A., 2012, *ApJ*, **745**, L11
- Fang X., Liu X.-W., 2011, *MNRAS*, **415**, 181
- Ferland G. J., et al., 2013, *Rev. Mex. Astron. Astrofis.*, **49**, 137
- Fishlock C. K., Karakas A. I., Lugaro M., Yong D., 2014, *ApJ*, **797**, 44
- Frew D. J., Bojčić I. S., Parker Q. A., 2013, *MNRAS*, **431**, 2
- Frew D. J., Parker Q. A., Bojčić I. S., 2016, *MNRAS*, **455**, 1459
- Gaia Collaboration et al., 2018, *A&A*, **616**, A1
- García-Hernández D. A., Manchado A., García-Lario P., Stanghellini L., Villaver E., Shaw R. A., Szczerba R., Perea-Calderón J. V., 2010, *ApJ*, **724**, L39
- García-Hernández D. A., Kameswara Rao N., Lambert D. L., 2011a, *ApJ*, **729**, 126
- García-Hernández D. A., et al., 2011b, *ApJ*, **737**, L30
- García-Hernández D. A., Villaver E., García-Lario P., Acosta-Pulido J. A., Manchado A., Stanghellini L., Shaw R. A., Cataldo F., 2012, *ApJ*, **760**, 107
- Gesicki K., Zijlstra A. A., 2007, *A&A*, **467**, L29
- Gielen C., et al., 2011a, *A&A*, **533**, A99
- Gielen C., Cami J., Bouwman J., Peeters E., Min M., 2011b, *A&A*, **536**, A54
- Gómez-Llanos V., Morisset C., Szczerba R., García-Hernández D. A., García-Lario P., 2018, preprint, ([arXiv:1806.10248](https://arxiv.org/abs/1806.10248))
- Henden A. A., Templeton M., Terrell D., Smith T. C., Levine S., Welch D., 2016, VizieR Online Data Catalog, **2336**
- Henry R. B. C., Kwitter K. B., Balick B., 2004, *AJ*, **127**, 2284
- Henry R. B. C., Kwitter K. B., Jaskot A. E., Balick B., Morrison M. A., Milingo J. B., 2010, *ApJ*, **724**, 748
- Houck J. R., et al., 2004, *ApJS*, **154**, 18
- Hubeny I., 1988, *Computer Physics Communications*, **52**, 103
- Hyung S., Aller L. H., Feibelman W. A., 1994, *PASP*, **106**, 745
- Ishihara D., et al., 2010, *A&A*, **514**, A1
- Izzard R. G., Tout C. A., Karakas A. I., Pols O. R., 2004, *MNRAS*, **350**, 407
- Karakas A. I., 2010, *MNRAS*, **403**, 1413
- Khan I., Worthey G., 2018, *A&A*, **615**, A115
- Kobayashi C., Karakas A. I., Umeda H., 2011, *MNRAS*, **414**, 3231
- Lanz T., Hubeny I., 2007, *ApJS*, **169**, 83
- Lodders K., 2010, in Goswami A., Reddy B. E., eds, *Principles and Perspectives in Cosmochemistry*. p. 379 ([arXiv:1010.2746](https://arxiv.org/abs/1010.2746)), doi:10.1007/978-3-642-10352-0_8
- Lumsden S. L., Puxley P. J., Hoare M. G., 2001, *MNRAS*, **328**, 419
- Martin P. G., Rouleau F., 1991, in Malina R. F., Bowyer S., eds, *Extreme Ultraviolet Astronomy*. p. 341
- Meixner M., et al., 2010, *PASP*, **122**, 451
- Méndez R. H., 1989, in Torres-Peimbert S., ed., *IAU Symposium Vol. 131, Planetary Nebulae*. pp 261–272
- Méndez R. H., Forte J. C., López R. H., 1986, *Rev. Mex. Astron. Astrofis.*, **13**, 119
- Mendez R. H., Kudritzki R. P., Herrero A., 1992, *A&A*, **260**, 329
- Miller T. R., Henry R. B. C., Balick B., Kwitter K. B., Dufour R. J., Shaw R. A., Corradi R. L. M., 2018, *MNRAS*,
- Morisset C., Georgiev L., 2009, *A&A*, **507**, 1517
- Noguchi K., et al., 2002, *PASJ*, **54**, 855
- Otsuka M., 2015, *MNRAS*, **452**, 4070
- Otsuka M., Tajitsu A., 2013, *ApJ*, **778**, 146
- Otsuka M., Tajitsu A., Hyung S., Izumiura H., 2010, *ApJ*, **723**, 658
- Otsuka M., Kemper F., Hyung S., Sargent B. A., Meixner M., Tajitsu A., Yanagisawa K., 2013, *ApJ*, **764**, 77
- Otsuka M., Kemper F., Cami J., Peeters E., Bernard-Salas J., 2014, *MNRAS*, **437**, 2577
- Otsuka M., Hyung S., Tajitsu A., 2015, *ApJS*, **217**, 22
- Otsuka M., et al., 2016, *MNRAS*, **462**, 12
- Peimbert M., 1978, in Terzian Y., ed., *IAU Symposium Vol. 76, Planetary Nebulae*. pp 215–223
- Peimbert M., Costero R., 1969, *Boletín de los Observatorios Tonantzintla y Tacubaya*, **5**, 3
- Pereira C.-B., Miranda L.-F., 2007, *A&A*, **467**, 1249
- Pottasch S. R., Bernard-Salas J., 2010, *A&A*, **517**, A95
- Pottasch S. R., Surendiranath R., Bernard-Salas J., 2011, *A&A*, **531**, A23
- Quireza C., Rocha-Pinto H. J., Maciel W. J., 2007, *A&A*, **475**, 217
- Rauch T., 2003, *A&A*, **403**, 709
- Roberts K. R. G., Smith K. T., Sarre P. J., 2012, *MNRAS*, **421**, 3277
- Sanduleak N., Stephenson C. B., 1972, *ApJ*, **178**, 183
- Sellgren K., Werner M. W., Ingalls J. G., Smith J. D. T., Carleton T. M., Joblin C., 2010, *ApJ*, **722**, L54
- Storey P. J., Hummer D. G., 1995, *MNRAS*, **272**, 41
- Tylenda R., Acker A., Stenholm B., Koepfen J., 1992, *A&AS*, **95**, 337
- Vassiliadis E., Wood P. R., 1994, *ApJS*, **92**, 125
- Wang W., Liu X.-W., 2007, *MNRAS*, **381**, 669
- Wegner W., 2003, *Astronomische Nachrichten*, **324**, 219
- Wolff M. J., Code A. D., Groth E. J., 2000, *AJ*, **119**, 302
- Zhang C. Y., 1995, *ApJS*, **98**, 659
- Zhang Y., Kwok S., 2011, *ApJ*, **730**, 126
- van de Steene G. C., Zijlstra A. A., 1995, *A&A*, **293**, 541

APPENDIX A: SUPPORTING RESULTS

The following tables and figure support our works.

Table A1. Identified emission lines in the HDS and IRS spectra. $f(\lambda)$ is reddening law of [Cardelli et al. \(1989\)](#), $F(\lambda)$ and $I(\lambda)$ are observed and interstellar extinction corrected line fluxes normalised to $F(\text{H}\beta)$ and $I(\text{H}\beta)$, respectively.

$\lambda_{\text{lab.}}$ (Å)	Line	$f(\lambda)$	$F(\lambda)$	$\delta F(\lambda)$	$I(\lambda)$	$\delta I(\lambda)$
3656.66	B37	0.336	0.015	0.010	0.019	0.013
3657.27	B36	0.336	0.062	0.019	0.077	0.024
3657.92	B35	0.336	0.048	0.013	0.060	0.017
3658.64	B34	0.336	0.076	0.012	0.094	0.017
3659.42	B32	0.336	0.131	0.015	0.162	0.023
3660.28	B33	0.335	0.162	0.014	0.201	0.024
3661.22	B31	0.335	0.265	0.021	0.330	0.038
3662.26	B30	0.335	0.324	0.028	0.402	0.048
3663.40	B29	0.335	0.377	0.032	0.469	0.055
3664.68	B28	0.334	0.762	0.052	0.945	0.101
3666.09	B27	0.334	0.676	0.049	0.839	0.092
3667.68	B26	0.334	0.623	0.039	0.773	0.080
3669.46	B25	0.334	0.581	0.032	0.721	0.071
3671.48	B24	0.333	0.593	0.029	0.735	0.070
3673.76	B23	0.333	0.733	0.030	0.909	0.083
3676.36	B22	0.332	0.739	0.033	0.916	0.085
3679.35	B21	0.332	0.844	0.031	1.046	0.094
3682.81	B20	0.331	0.897	0.034	1.111	0.100
3686.83	B19	0.330	1.121	0.031	1.388	0.119
3691.55	B18	0.329	1.184	0.023	1.465	0.122
3697.15	B17	0.328	1.298	0.027	1.605	0.134
3703.85	B16	0.327	1.778	0.031	2.196	0.181
3709.65	He I	0.326	0.039	0.013	0.049	0.016
3711.97	B15	0.325	1.665	0.032	2.054	0.169
3721.94	B14	0.323	2.167	0.040	2.671	0.218
3726.03	[O II]	0.322	107.494	1.338	132.411	10.617
3728.81	[O II]	0.322	74.678	0.644	91.955	7.314
3733.01	He I	0.321	0.071	0.010	0.088	0.014
3734.37	B13	0.321	2.375	0.036	2.922	0.235
3750.15	B12	0.317	3.125	0.027	3.836	0.301
3770.63	B11	0.313	4.076	0.033	4.991	0.386
3797.90	B10	0.307	5.102	0.035	6.224	0.472
3819.60	He I	0.302	0.089	0.011	0.108	0.015
3835.38	B9 (H γ)	0.299	6.491	0.037	7.876	0.580
3889.05	B8	0.286	9.595	0.191	11.547	0.844
3918.97	C II	0.279	0.065	0.011	0.078	0.014
3920.68	C II	0.279	0.142	0.011	0.170	0.018
3970.07	B7 (He)	0.266	14.294	0.071	16.977	1.113
4068.60	[S II]	0.239	0.808	0.035	0.944	0.069
4101.73	B6 (H δ)	0.230	23.318	0.106	27.051	1.531
4267.00	C II	0.180	0.210	0.030	0.236	0.035
4340.46	B5 (H γ)	0.157	42.854	0.195	47.420	1.837
4471.47	He I	0.115	0.569	0.013	0.613	0.022
4571.10	Mg I	0.084	0.106	0.019	0.112	0.020
4658.05	[Fe III]	0.058	0.391	0.015	0.406	0.017
4701.53	[Fe III]	0.045	0.093	0.008	0.096	0.009
4754.69	[Fe III]	0.030	0.077	0.013	0.079	0.014
4769.43	[Fe III]	0.025	0.025	0.008	0.025	0.008
4861.33	B4 (H β)	0.000	100.000	0.251	100.000	0.251
4881.00	[Fe III]	-0.005	0.131	0.009	0.130	0.009
4888.87	[Fe III]	-0.007	0.021	0.007	0.021	0.007
4921.93	He I	-0.016	0.130	0.008	0.129	0.008
4958.91	[O III]	-0.026	1.127	0.008	1.109	0.011
5006.84	[O III]	-0.038	3.408	0.015	3.326	0.034
5015.68	He I	-0.040	0.385	0.010	0.375	0.011
5055.98	Si II	-0.050	0.097	0.031	0.094	0.030
5067.52	Ni III	-0.052	0.065	0.010	0.062	0.009
5197.90	[N I]	-0.082	0.059	0.022	0.056	0.021
5200.26	[N I]	-0.083	0.055	0.015	0.052	0.014
5270.40	[Fe III]	-0.098	0.183	0.011	0.172	0.011
5273.24	Ne II	-0.098	0.031	0.012	0.029	0.011
5517.72	[Cl III]	-0.145	0.128	0.013	0.116	0.012
5537.89	[Cl III]	-0.149	0.122	0.006	0.111	0.007
5754.64	[N II]	-0.185	1.489	0.017	1.322	0.062
5875.60	He I	-0.203	1.786	0.029	1.566	0.082
5886.05	C II	-0.205	0.061	0.010	0.054	0.009
5891.60	C II	-0.205	0.056	0.008	0.049	0.007
5912.58	C I	-0.208	0.058	0.005	0.051	0.005
5931.78	N II	-0.211	0.068	0.008	0.059	0.007
5950.71	Fe III	-0.214	0.040	0.009	0.035	0.008
6300.30	[O I]	-0.263	0.638	0.018	0.538	0.038
6312.10	[S III]	-0.264	0.212	0.013	0.179	0.016
6347.03	Ni II	-0.269	0.070	0.010	0.059	0.009
6363.78	[O I]	-0.271	0.195	0.014	0.164	0.016

Table A1. Continued.

$\lambda_{\text{lab.}}$ (Å)	Line	$f(\lambda)$	$F(\lambda)$	$\delta F(\lambda)$	$I(\lambda)$	$\delta I(\lambda)$
6379.58	O II	-0.273	0.098	0.023	0.082	0.020
6461.95	C II	-0.284	0.074	0.009	0.061	0.008
6548.04	[N II]	-0.296	45.988	0.395	37.985	2.778
6562.80	B3 (H α)	-0.298	375.888	1.958	310.085	22.731
6578.05	C II	-0.300	0.317	0.008	0.261	0.020
6583.46	[N II]	-0.300	138.238	1.323	113.836	8.471
6678.15	He I	-0.313	0.588	0.012	0.480	0.038
6716.44	[S II]	-0.318	4.770	0.047	3.884	0.306
6730.81	[S II]	-0.320	7.203	0.078	5.857	0.465
7065.18	He I	-0.364	0.494	0.011	0.391	0.036
7135.80	[Ar III]	-0.374	0.740	0.009	0.581	0.054
7231.32	C II	-0.387	0.352	0.018	0.274	0.024
7236.42	C II	-0.387	0.741	0.034	0.576	0.042
7281.35	He I	-0.393	0.159	0.010	0.123	0.014
7318.92	[O II]	-0.398	1.465	0.061	1.132	0.120
7319.99	[O II]	-0.398	4.560	0.057	3.524	0.348
7329.66	[O II]	-0.400	2.382	0.026	1.839	0.182
7330.73	[O II]	-0.400	2.460	0.029	1.899	0.188
7751.10	[Ar III]	-0.455	0.187	0.009	0.139	0.017
7769.23	Ca I	-0.458	0.122	0.007	0.091	0.012
7771.94	O I	-0.458	0.084	0.006	0.063	0.008
7874.65	[Fe II]	-0.471	0.032	0.004	0.023	0.004
8240.19	P45	-0.515	0.067	0.008	0.048	0.008
8241.88	P44	-0.516	0.090	0.008	0.064	0.010
8243.69	P43	-0.516	0.055	0.006	0.039	0.007
8245.64	P42	-0.516	0.023	0.005	0.016	0.004
8247.73	P41	-0.516	0.071	0.006	0.051	0.008
8249.97	P40	-0.517	0.037	0.003	0.027	0.004
8252.40	P39	-0.517	0.077	0.008	0.055	0.009
8255.02	P38	-0.517	0.093	0.008	0.066	0.010
8257.85	P37	-0.517	0.093	0.007	0.066	0.010
8260.93	P36	-0.518	0.103	0.010	0.074	0.012
8264.28	P35	-0.518	0.107	0.009	0.076	0.012
8267.94	P34	-0.519	0.114	0.008	0.082	0.012
8271.93	P33	-0.519	0.118	0.012	0.084	0.014
8276.31	P32	-0.520	0.120	0.011	0.086	0.014
8281.12	P31	-0.520	0.114	0.010	0.081	0.013
8286.43	P30	-0.521	0.135	0.011	0.096	0.015
8292.31	P29	-0.521	0.190	0.012	0.135	0.019
8298.83	P28	-0.522	0.164	0.010	0.117	0.017
8306.11	P27	-0.523	0.207	0.012	0.148	0.021
8333.78	P24	-0.526	0.307	0.017	0.218	0.031
8340.80	C II	-0.527	0.018	0.005	0.013	0.004
8345.47	P23	-0.527	0.296	0.017	0.211	0.030
8359.00	P22	-0.529	0.385	0.021	0.274	0.038
8374.48	P21	-0.531	0.366	0.020	0.260	0.037
8392.40	P20	-0.533	0.382	0.020	0.271	0.038
8413.32	P19	-0.535	0.449	0.021	0.318	0.044
8502.48	P16	-0.544	0.668	0.031	0.470	0.067
8665.02	P13	-0.560	1.274	0.057	0.887	0.128
8750.47	P12	-0.568	1.558	0.069	1.079	0.158
8776.83	He I	-0.571	0.046	0.005	0.032	0.006
8862.78	P11	-0.578	1.903	0.085	1.309	0.195
9014.91	P10	-0.590	2.554	0.113	1.744	0.264
9068.60	[S III]	-0.594	3.789	0.170	2.581	0.394
9123.60	[Cl II]	-0.598	0.128	0.010	0.087	0.014
9545.97	P8	-0.626	4.546	0.202	3.033	0.486

Table A1. Continued.

$\lambda_{\text{lab.}}$ (Å)	Line	$f(\lambda)$	$F(\lambda)$	$\delta F(\lambda)$	$I(\lambda)$	$\delta I(\lambda)$
70000.0	C ₆₀ /[Ar II]/H I				28.665	3.226
74578.2	H I				3.102	0.226
85000.0	C ₆₀				7.003	0.545
89889.3	[Ar III]				0.757	0.145
123800.0	H I				1.029	0.271
128100.6	[Ne II]				20.607	1.555
174000.0	C ₆₀ /C ₇₀				12.131	1.654
	C ₆₀				9.399	1.282
187079.3	[S III]				5.263	0.724
189000.0	C ₆₀ /C ₇₀				< 21.253	
	C ₆₀				< 19.188	
334719.0	[S III]				4.004	0.857

Note – We measured the flux of the C_{60,70} 18.9 μm by adopting FWHM of 0.347 μm measured in Tc 1 (Otsuka et al. 2014) because this line seems to be partially lacked due to spike noise. We estimated the expected solo intensity of the C₆₀ 17.4/18.9 μm using the C₆₀/C₇₀ ratio at 17.4 μm = 3.44 and the C₆₀/C₇₀ ratio at 18.9 μm = 9.29 measured in Tc 1 (Cami et al. 2010).

Table A2. Broadband flux density of SaSt 2-3.

Band	λ_c	F_λ (reddened) (erg s ⁻¹ cm ⁻² μm^{-1})	I_λ (de-reddened) (erg s ⁻¹ cm ⁻² μm^{-1})
<i>B</i>	0.4297 μm	2.24(-10) \pm 5.99(-12)	4.75(-10) \pm 1.41(-10)
<i>g'</i>	0.4640 μm	1.93(-10) \pm 1.42(-12)	3.81(-10) \pm 1.03(-10)
<i>V</i>	0.5394 μm	1.31(-10) \pm 3.25(-12)	2.29(-10) \pm 5.14(-11)
<i>r'</i>	0.6122 μm	1.05(-10) \pm 2.61(-12)	1.96(-10) \pm 3.82(-11)
<i>i'</i>	0.7440 μm	3.89(-11) \pm 3.29(-12)	7.89(-11) \pm 1.35(-11)
<i>J</i>	1.235 μm	1.27(-11) \pm 3.03(-13)	1.48(-11) \pm 9.94(-13)
<i>H</i>	1.662 μm	4.49(-12) \pm 1.24(-13)	4.95(-12) \pm 2.36(-13)
<i>Ks</i>	2.159 μm	2.01(-12) \pm 6.86(-14)	2.15(-12) \pm 9.13(-14)
<i>Bry</i>	2.162 μm	4.29(-12) \pm 7.66(-13)	4.57(-12) \pm 8.25(-13)
<i>Bry45</i>	2.188 μm	2.15(-12) \pm 4.14(-14)	2.28(-12) \pm 7.21(-14)
<i>W1</i>	3.353 μm		9.28(-13) \pm 1.97(-14)
<i>W2</i>	4.602 μm		7.49(-13) \pm 1.45(-14)
<i>W3</i>	11.56 μm		7.87(-13) \pm 1.09(-14)
<i>L18W</i>	18.00 μm		1.40(-12) \pm 3.71(-13)
<i>W4</i>	22.09 μm		1.50(-12) \pm 3.04(-14)

Table A3. Ionic abundances of SaSt 2-3 using nebular emission lines.

Ion(X ^{m+})	$\lambda_{\text{lab.}}$	$I(\lambda)$ ($I(\text{H}\beta) = 100$)	$n(\text{X}^{\text{m+}})/n(\text{H}^+)$	
He ⁺	4471.47 Å	0.613 \pm 0.022	1.11(-2) \pm 4.43(-4)	
	4921.93 Å	0.129 \pm 0.008	9.44(-3) \pm 6.10(-4)	
	5015.68 Å	0.375 \pm 0.011	1.20(-2) \pm 4.04(-4)	
	5875.60 Å	1.566 \pm 0.082	9.58(-3) \pm 5.33(-4)	
	6678.15 Å	0.480 \pm 0.038	1.19(-2) \pm 9.72(-4)	
	7065.18 Å	0.391 \pm 0.036	6.49(-3) \pm 6.06(-4)	
	7281.35 Å	0.123 \pm 0.014	1.06(-2) \pm 1.21(-3)	
			1.09(-2) \pm 2.28(-4)	
	C ²⁺	4267.00 Å	0.236 \pm 0.035	2.39(-4) \pm 3.58(-5)
		5891.60 Å	0.049 \pm 0.007	3.35(-4) \pm 4.56(-5)
6461.95 Å		0.061 \pm 0.008	6.03(-4) \pm 8.07(-5)	
6578.05 Å		0.261 \pm 0.020	3.16(-4) \pm 2.60(-5)	
7231.34 Å		0.274 \pm 0.024	6.11(-4) \pm 8.85(-5)	
7236.42 Å		0.576 \pm 0.042	6.68(-4) \pm 6.13(-5)	
			3.14(-4) \pm 2.49(-5)	
N ⁰	5197.90 Å	0.056 \pm 0.021	7.60(-7) \pm 2.85(-7)	
	5200.26 Å	0.052 \pm 0.014	4.04(-7) \pm 1.35(-7)	
			5.82(-7) \pm 2.51(-7)	
N ⁺	5754.64 Å	1.322 \pm 0.062	2.88(-5) \pm 5.08(-6)	
	6548.04 Å	37.985 \pm 2.778	2.83(-5) \pm 2.93(-6)	
	6583.46 Å	113.836 \pm 8.471	2.86(-5) \pm 3.00(-6)	
			2.85(-5) \pm 1.94(-6)	
O ⁰	6300.30 Å	0.538 \pm 0.038	4.37(-6) \pm 1.25(-6)	
	6363.78 Å	0.164 \pm 0.016	4.16(-6) \pm 1.22(-6)	
			4.26(-6) \pm 8.72(-7)	
O ⁺	3726.03 Å	132.411 \pm 10.617	1.29(-4) \pm 2.56(-5)	
	3728.81 Å	91.955 \pm 7.314	1.25(-4) \pm 1.38(-5)	
	7318.92 Å	1.132 \pm 0.120	1.38(-4) \pm 5.23(-5)	
	7319.99 Å	3.524 \pm 0.348	1.37(-4) \pm 5.16(-5)	
	7329.66 Å	1.839 \pm 0.182	1.35(-4) \pm 5.11(-5)	
	7330.73 Å	1.899 \pm 0.188	1.41(-4) \pm 5.31(-5)	
			1.28(-4) \pm 1.10(-5)	
O ²⁺	4958.91 Å	1.109 \pm 0.011	1.68(-6) \pm 6.82(-7)	
	5006.84 Å	3.326 \pm 0.034	1.75(-6) \pm 7.08(-7)	
			1.72(-6) \pm 4.91(-7)	
Ne ⁺	12.81 μm	20.607 \pm 1.555	2.91(-5) \pm 2.85(-6)	
	4068.60 Å	0.944 \pm 0.069	6.22(-7) \pm 1.08(-7)	
	6716.44 Å	3.884 \pm 0.306	6.47(-7) \pm 6.72(-8)	
	6730.81 Å	5.857 \pm 0.465	6.38(-7) \pm 7.27(-8)	
			6.39(-7) \pm 4.49(-8)	
S ²⁺	18.71 μm	5.263 \pm 0.724	6.08(-7) \pm 9.80(-8)	
	33.47 μm	4.004 \pm 0.857	5.93(-7) \pm 1.63(-7)	
	6312.10 Å	0.179 \pm 0.016	5.84(-7) \pm 3.00(-7)	
	9068.60 Å	2.581 \pm 0.394	7.28(-7) \pm 2.17(-7)	
			6.18(-7) \pm 7.57(-8)	
Cl ⁺	9123.60 Å	0.087 \pm 0.014	1.74(-8) \pm 3.20(-9)	
	5517.72 Å	0.116 \pm 0.012	2.12(-8) \pm 8.45(-9)	
	5537.89 Å	0.111 \pm 0.007	1.87(-8) \pm 5.29(-9)	
			1.94(-8) \pm 4.48(-9)	
Ar ²⁺	8.99 μm	0.757 \pm 0.145	8.79(-8) \pm 1.74(-8)	
	7135.80 Å	0.581 \pm 0.054	9.30(-8) \pm 2.58(-8)	
	7751.10 Å	0.139 \pm 0.017	9.29(-8) \pm 2.68(-8)	
			9.02(-8) \pm 1.27(-8)	
Fe ²	4658.05 Å	0.406 \pm 0.017	1.93(-7) \pm 2.49(-8)	
	4701.53 Å	0.096 \pm 0.009	1.45(-7) \pm 2.40(-8)	
	4754.69 Å	0.079 \pm 0.014	2.00(-7) \pm 4.24(-8)	
	4769.43 Å	0.025 \pm 0.008	1.10(-7) \pm 3.71(-8)	
	4881.00 Å	0.130 \pm 0.009	1.09(-7) \pm 1.99(-8)	
	5270.40 Å	0.172 \pm 0.011	1.61(-7) \pm 2.06(-8)	
			1.48(-7) \pm 1.03(-8)	

Table A4. The measurements of the equivalent width (*EW*) of the stellar absorption and the derived elemental abundances.

Line	λ_{lab} (Å)	<i>EW</i> (mÅ)	$n(\text{X})/n(\text{H})$	$\epsilon(\text{X})$
He I	3652.90	29.24 ± 1.87	$8.92(-2) \pm 2.77(-2)$	10.95 ± 0.14
	3867.45	104.20 ± 1.30	$9.30(-2) \pm 1.41(-2)$	10.97 ± 0.07
	4009.24	188.70 ± 1.56	$7.85(-2) \pm 9.76(-3)$	10.89 ± 0.05
	4120.78	184.40 ± 2.10	$1.20(-1) \pm 2.12(-2)$	11.08 ± 0.08
	4143.68	266.70 ± 1.65	$1.13(-1) \pm 1.47(-2)$	11.05 ± 0.06
He II	4168.99	39.69 ± 1.48	$8.60(-2) \pm 1.96(-2)$	10.93 ± 0.10
	4541.62	129.90 ± 2.34	$1.01(-1) \pm 2.23(-2)$	11.01 ± 0.10
	4685.71	210.00 ± 1.96	$9.85(-2) \pm 2.12(-2)$	10.99 ± 0.09
C III	5411.52	136.90 ± 2.21	$9.85(-2) \pm 2.27(-2)$	10.99 ± 0.10
			$9.76(-2) \pm 1.93(-3)$	10.99 ± 0.09
	4156.56	65.84 ± 1.68	$3.83(-4) \pm 8.75(-5)$	8.58 ± 0.10
	4162.96	75.54 ± 1.79	$3.39(-4) \pm 7.42(-5)$	8.53 ± 0.10
C IV	4665.92	67.63 ± 1.49	$3.47(-4) \pm 7.07(-5)$	8.54 ± 0.09
	5801.31	44.60 ± 1.60	$3.96(-4) \pm 1.12(-4)$	8.60 ± 0.12
N II			$3.66(-4) \pm 8.60(-5)$	8.56 ± 0.10
	3995.00	15.58 ± 1.45	$1.68(-5) \pm 7.90(-6)$	7.23 ± 0.20
N III	4634.12	26.21 ± 1.47	$1.91(-5) \pm 5.61(-6)$	7.28 ± 0.13
			$1.85(-5) \pm 6.76(-6)$	7.25 ± 0.16
O II	3882.17	38.17 ± 1.34	$8.77(-5) \pm 3.08(-5)$	7.94 ± 0.15
	3954.21	37.06 ± 0.93	$1.66(-4) \pm 3.19(-5)$	8.22 ± 0.08
	3982.72	26.86 ± 1.89	$8.70(-5) \pm 5.19(-5)$	7.94 ± 0.26
	4092.89	22.34 ± 1.23	$6.36(-5) \pm 4.62(-5)$	7.80 ± 0.32
	4119.22	54.49 ± 1.67	$1.38(-4) \pm 2.93(-5)$	8.14 ± 0.09
	4132.79	24.40 ± 1.15	$1.99(-4) \pm 4.91(-5)$	8.30 ± 0.11
	4189.75	30.55 ± 1.22	$2.24(-4) \pm 4.86(-5)$	8.35 ± 0.09
	4366.77	53.74 ± 1.13	$1.07(-4) \pm 1.92(-5)$	8.07 ± 0.08
	4590.83	63.35 ± 2.44	$8.57(-5) \pm 2.01(-5)$	7.93 ± 0.10
	4596.07	62.17 ± 1.51	$1.07(-4) \pm 1.92(-5)$	8.03 ± 0.08
	4661.53	61.34 ± 1.25	$1.07(-4) \pm 2.35(-5)$	8.16 ± 0.06
	4673.84	10.44 ± 1.19	$1.43(-4) \pm 5.31(-5)$	7.89 ± 0.30
	4676.14	45.04 ± 1.22	$7.75(-5) \pm 2.30(-5)$	8.10 ± 0.08
			$1.25(-4) \pm 4.86(-5)$	8.10 ± 0.17
Si III	4552.57	83.11 ± 1.22	$6.61(-6) \pm 9.81(-7)$	6.82 ± 0.06
	4567.77	62.27 ± 1.10	$7.33(-6) \pm 1.14(-6)$	6.87 ± 0.07
	4574.57	21.00 ± 1.31	$5.90(-6) \pm 1.65(-6)$	6.77 ± 0.12
Si IV	4116.11	162.50 ± 1.29	$4.33(-6) \pm 6.08(-7)$	6.64 ± 0.06
	4631.08	42.81 ± 2.00	$8.41(-6) \pm 2.47(-6)$	6.93 ± 0.13
			$6.52(-6) \pm 1.54(-6)$	6.81 ± 0.10

Table A5. Comparison of the observed line intensities, band fluxes, and flux densities between the CLOUDY model and the observation. The band width for the integrated band flux is as follows: 0.084, 0.116, 0.087, 0.111, 0.104 μm in B , g' , V , r' , and i' , respectively. 0.162, 0.251, 0.260, 0.626, 1.042 μm in J , H , K_s , $W1$, and $W2$, respectively. 0.36, 0.40, 0.60, 1.00, 0.25, 1.00, 2.00, 0.70, 0.40, 0.50, 0.50, 0.50, 0.50, and 1.00 μm in IRS-1 to -15, respectively.

Line	λ_{lab}	$I(\text{CLOUDY})$ $I(\text{H}\beta)=100$	$I(\text{Obs})$ $I(\text{H}\beta)=100$	Line	λ_{lab}	$I(\text{CLOUDY})$ $I(\text{H}\beta)=100$	$I(\text{Obs})$ $I(\text{H}\beta)=100$
B24	3671 Å	0.439	0.735	[Cl III]	5538 Å	0.122	0.111
B23	3674 Å	0.487	0.909	[N II]	5755 Å	1.293	1.322
B22	3676 Å	0.545	0.916	He I	5876 Å	1.673	1.566
B21	3679 Å	0.613	1.046	[O I]	6300 Å	0.951	0.538
B20	3683 Å	0.696	1.111	[S III]	6312 Å	0.392	0.179
B19	3687 Å	0.798	1.388	[O I]	6363 Å	0.303	0.164
B18	3692 Å	0.924	1.465	[N II]	6548 Å	35.039	37.985
B17	3697 Å	1.081	1.605	B3	6563 Å	289.424	310.085
B16	3704 Å	1.282	2.196	[N II]	6584 Å	103.400	113.836
B15	3712 Å	1.541	2.054	He I	6678 Å	0.467	0.480
B14	3722 Å	1.882	2.671	[S II]	6716 Å	2.688	3.884
[O II]	3726 Å	139.511	132.411	[S II]	6731 Å	4.311	5.857
[O II]	3729 Å	76.585	91.955	He I	7065 Å	0.541	0.391
B13	3734 Å	2.340	2.922	[Ar III]	7135 Å	0.592	0.581
B12	3750 Å	2.966	3.836	He I	7281 Å	0.110	0.123
B11	3771 Å	3.849	4.991	[O II]	7323 Å	6.193	4.657
B10	3798 Å	5.130	6.224	[O II]	7332 Å	4.939	3.739
He I	3820 Å	0.138	0.108	[Ar III]	7751 Å	0.143	0.139
B9	3835 Å	7.068	7.876	P24	8334 Å	0.145	0.218
B8	3889 Å	10.143	11.547	P23	8346 Å	0.162	0.211
B7	3970 Å	15.359	16.977	P22	8359 Å	0.182	0.274
[S II]	4070 Å	1.019	0.944	P21	8374 Å	0.206	0.260
B6	4102 Å	25.012	27.051	P20	8392 Å	0.235	0.271
B5	4340 Å	45.252	47.420	P19	8413 Å	0.271	0.318
He I	4471 Å	0.556	0.613	P16	8502 Å	0.441	0.470
[Fe III]	4659 Å	0.323	0.401	P13	8665 Å	0.815	0.887
[Fe III]	4702 Å	0.108	0.112	P12	8750 Å	1.036	1.079
[Fe III]	4755 Å	0.059	0.079	P11	8863 Å	1.347	1.309
[Fe III]	4770 Å	0.036	0.025	P10	9015 Å	1.798	1.744
[Fe III]	4881 Å	0.106	0.130	[S III]	9069 Å	4.858	2.581
He I	4922 Å	0.155	0.129	[Cl II]	9124 Å	0.058	0.087
[O III]	4959 Å	1.095	1.109	P8	9546 Å	3.568	3.033
[O III]	5007 Å	3.296	3.326	H I	7.48/50 μm	3.153	3.102
He I	5016 Å	0.427	0.375	[Ar III]	8.99 μm	0.618	0.757
[N I]	5198 Å	0.036	0.056	H I	12.38 μm	1.067	1.029
[N I]	5200 Å	0.022	0.052	[Ne II]	12.81 μm	20.002	20.607
[Fe III]	5271 Å	0.187	0.172	[S III]	18.71 μm	6.684	5.263
[Cl III]	5518 Å	0.113	0.116	[S III]	33.47 μm	2.941	4.004
Band	λ_c	$I(\text{CLOUDY})$ $I(\text{H}\beta)=100$	$I(\text{Obs})$ $I(\text{H}\beta)=100$	Band	λ_c	$I(\text{CLOUDY})$ $I(\text{H}\beta)=100$	$I(\text{Obs})$ $I(\text{H}\beta)=100$
B	0.4297 μm	3112.550	2569.843	IRS-04	14.50 μm	42.844	53.079
g'	0.4640 μm	3502.697	2831.786	IRS-05	15.00 μm	11.085	13.975
V	0.5394 μm	1401.690	1280.855	IRS-06	16.50 μm	50.613	64.398
r'	0.6122 μm	2097.757	1395.011	IRS-07	22.00 μm	145.937	177.499
i'	0.7440 μm	603.378	527.513	IRS-08	23.35 μm	53.640	64.324
J	1.235 μm	168.908	153.285	IRS-09	27.00 μm	32.776	37.026
H	1.662 μm	82.062	79.281	IRS-10	28.00 μm	41.138	45.412
K_s	2.159 μm	45.506	35.859	IRS-11	29.00 μm	40.587	44.158
$W1$	3.353 μm	38.985	36.990	IRS-12	30.00 μm	39.898	42.550
$W2$	4.603 μm	43.688	49.748	IRS-13	31.00 μm	38.834	40.629
IRS-01	8.100 μm	10.832	10.822	IRS-14	32.00 μm	37.647	38.441
IRS-02	10.00 μm	12.494	13.062	IRS-15	34.50 μm	73.392	64.405
IRS-03	13.50 μm	23.575	28.543				
ID	λ_c	$F_\nu(\text{CLOUDY})$ (Jy)	$F_\nu(\text{Model})$ (Jy)	ID	λ_c	$F_\nu(\text{CLOUDY})$ (Jy)	$F_\nu(\text{Model})$ (Jy)
MIR-01	15.00 μm	0.052	0.066	FIR-02	90.00 μm	0.081	0.063
MIR-02	20.00 μm	0.135	0.172	FIR-03	100.0 μm	0.060	0.052
MIR-03	25.00 μm	0.262	0.306	FIR-04	120.0 μm	0.035	0.035
MIR-04	30.00 μm	0.375	0.401	FIR-05	140.0 μm	0.023	0.025
FIR-01	65.00 μm	0.201	0.105				

This paper has been typeset from a \TeX/L\AA\TeX file prepared by the author.

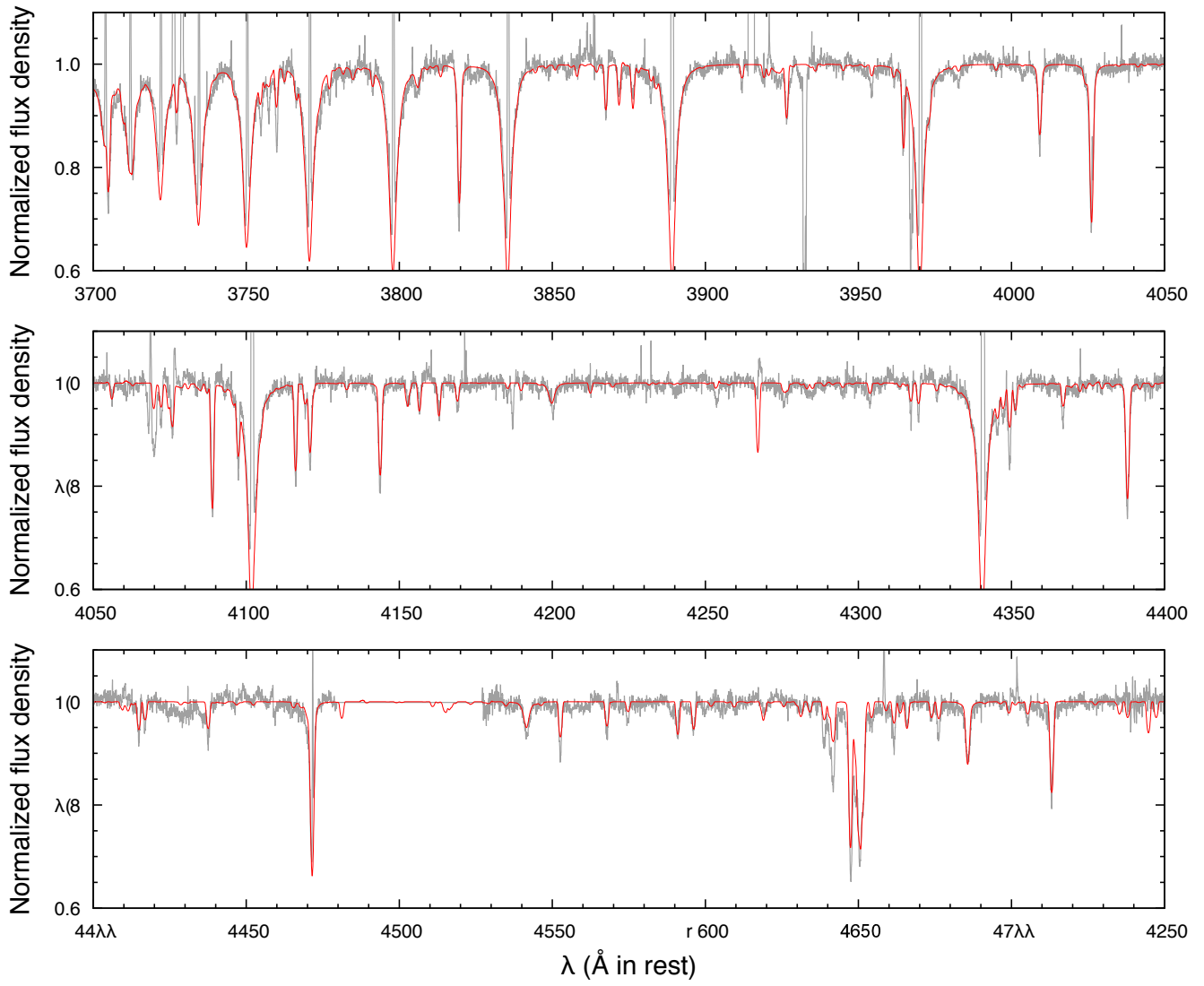


Figure A1. Comparison between the observed HDS (grey line) and the TLUSTY synthetic spectrum (red line) of SaSt 2-3. The input parameters are listed in Table 5.